Cell Stem Cell

Article

Patient-derived organoids model cervical tissue dynamics and viral oncogenesis in cervical cancer

Graphical abstract

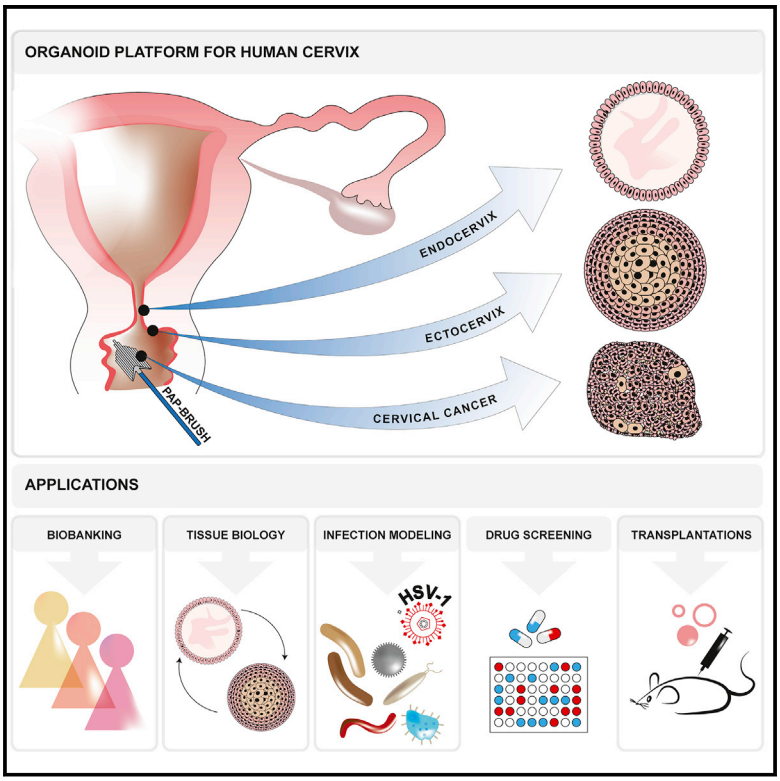

Highlights

- Establishment of long-term organoid cultures from human ecto- and endocervix
- Promising platform for modeling STIs, as evidenced for HSV-1
- Pap brush collection as a successful method for cervical tumoroid derivation
- Cervical tumoroids display disease hallmarks, such as causative HPV infection

Authors

Kadi Lõhmussaar, Rurika Oka, Jose Espejo Valle-Inclan, ..., Sebastiaan Veersema, Ruben van Boxtel, Hans Clevers

Correspondence

h.clevers@hubrecht.eu

In brief

Human-based model systems that faithfully recapitulate cervical cancer and causative HPV infection are scarce and often inadequate. With the advances in organoid technology, Lõhmussaar et al. have now extended this knowledge to the cervix, describing a successful derivation of endo- and ectocervical organoids as well as tumoroids from the associated malignancies.

Lõhmussaar et al., 2021, Cell Stem Cell *28*, 1–17
August 5, 2021
https://doi.org/10.1016/j.stem.2021.03.012

CellPress

Cell Stem Cell

CellPress

Article

Patient-derived organoids model cervical tissue dynamics and viral oncogenesis in cervical cancer

Kadi Lõhmussaar,[1,2] Rurika Oka,[2,9] Jose Espejo Valle-Inclan,[2,3] Milou H.H. Smits,[1] Hila Wardak,[1] Jeroen Korving,[1,2] Harry Begthel,[1,2] Natalie Proost,[4] Marieke van de Ven,[4] Onno W. Kranenburg,[5] Trudy G.N. Jonges,[6] Ronald P. Zweemer,[7] Sebastiaan Veersema,[8] Ruben van Boxtel,[2,9] and Hans Clevers[1,2,9,10,*]

[1]Hubrecht Institute, Royal Netherlands Academy of Arts and Sciences (KNAW) and University Medical Center (UMC) Utrecht, Uppsalalaan 8, 3584 CT Utrecht, the Netherlands

[2]Oncode Institute, Jaarbeursplein 6, 3521 AL Utrecht, the Netherlands

[3]Center for Molecular Medicine, UMC Utrecht, Utrecht University, Heidelberglaan 100, 3584 CX Utrecht, the Netherlands

[4]Preclinical Intervention Unit of the Mouse Clinic for Cancer and Ageing (MCCA) at the NKI, Plesmanlaan 121, 1066 CX, the Netherlands

[5]Utrecht Platform for Organoid Technology (U-PORT), UMC Utrecht, Utrecht University, Heidelberglaan 100, 3584 CX Utrecht, the Netherlands

[6]Department of Pathology, UMC Utrecht, Utrecht University, Heidelberglaan 100, 3584 CX Utrecht, the Netherlands

[7]Department of Gynaecological Oncology, Cancer Center, UMC Utrecht, Utrecht University, Heidelberglaan 100, 3584 CX Utrecht, the Netherlands

[8]Department of Reproductive Medicine and Gynaecology, Division Woman and Baby, UMC Utrecht, Heidelberglaan 100, 3584 CX Utrecht, the Netherlands

[9]Princess Máxima Center for Pediatric Oncology, Heidelberglaan 25, 3584 CS Utrecht, the Netherlands

[10]Lead contact

*Correspondence: h.clevers@hubrecht.eu

https://doi.org/10.1016/j.stem.2021.03.012

SUMMARY

Cervical cancer is a common gynecological malignancy often caused by high-risk human papillomavirus. There is a paucity of human-derived culture systems to study the cervical epithelium and the cancers derived thereof. Here we describe a long-term culturing protocol for ecto- and endocervical epithelia that generates 3D organoids that stably recapitulate the two tissues of origin. As evidenced for HSV-1, organoid-based cervical models may serve to study sexually transmitted infections. Starting from Pap brush material, a small biobank of tumoroids derived from affected individuals was established that retained the causative human papillomavirus (HPV) genomes. One of these uniquely carried the poorly characterized HPV30 subtype, implying a potential role in carcinogenesis. The tumoroids displayed differential responses to common chemotherapeutic agents and grew as xenografts in mice. This study describes an experimental platform for cervical (cancer) research and for future personalized medicine approaches.

INTRODUCTION

Once the deadliest cancer in the world, cervical cancer mortality rates have declined significantly since the discovery of the role of human papillomavirus (HPV) infection in cancer pathogenesis and development of successful screening strategies (Horn et al., 2019; Isidean et al., 2016; Ronco et al., 2014). Preventive care via vaccination at a young age, regular Papanicolaou (Pap) tests and additional HPV DNA testing have led to a reduction in the incidence of cervical cancer. However, in low-income countries with limited access to high-quality healthcare, cervical cancer remains the leading cause of death from cancer among women (Randall and Ghebre, 2016; Shrestha et al., 2018). Additionally, prophylactic vaccination is not mandatory and only effective when administered at a young age and does not protect against all oncogenic strains of the virus. Thus, challenges for better understanding the pathogenesis of cervical cancer and finding effective treatment strategies still remain.

The most common subtypes of cervical cancer are squamous cell carcinoma (SqCa) and adenocarcinoma (AdCa), which account for up to 70% and 25% of all cases, respectively (Cohen et al., 2019). These tumors arise from distinct regions of the uterine cervix: the outer ectocervical canal, inner endocervical canal, and transformation zone. The ectocervix is lined with stratified squamous epithelium and is the origin of SqCa, whereas the endocervix is composed of glandular columnar cells that can give rise to AdCa-s. The majority of SqCa-s is caused by sexually acquired infection with high-risk HPVs, such as HPV16 and HPV18 (Bosch et al., 2002). Viral tropism toward the ectocervix is associated with the dynamic life cycle of HPVs. The virus infects the proliferating basal cells of the stratified epithelium and requires the host cell's squamous differentiation for completion of its own life cycle (Kajitani et al., 2012). During productive infection in host cells, the virus expresses specific oncogenes (E6 and E7) that deregulate the cell cycle and, thus, promotes tumorigenesis (Androphy et al., 1987; Banks et al., 1987; Phelps et al., 1988; Schwarz et al., 1985).

Please cite this article in press as: Lõhmussaar et al., Patient-derived organoids model cervical tissue dynamics and viral oncogenesis in cervical cancer, Cell Stem Cell (2021), https://doi.org/10.1016/j.stem.2021.03.012

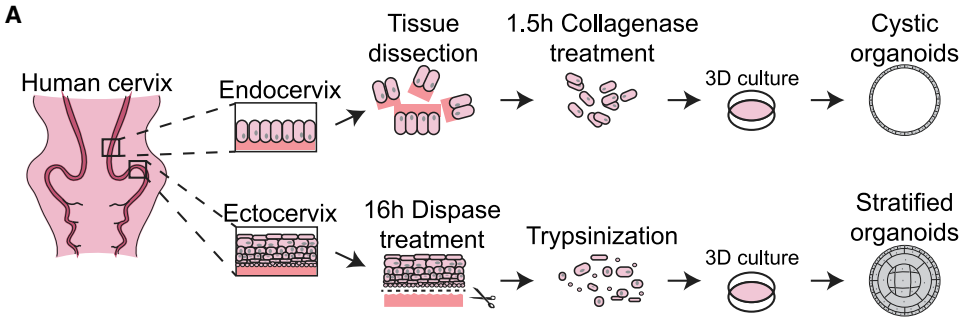

B

	M1	M2	M3	M4	M5	M6	M7
BASE	+	+	+	+	+	+	+
FGF7	-	+	+	+	+	+	+
NAC	-	-	+	+	+	+	+
A83	-	-	-	+	+	+	+
FSK	-	-	-	-	+	+	+
FGF10	-	-	-	-	-	+	+
RSPO1	-	-	-	-	-	-	+

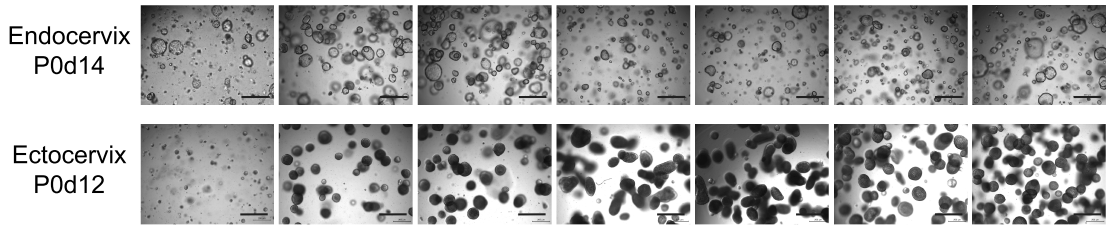

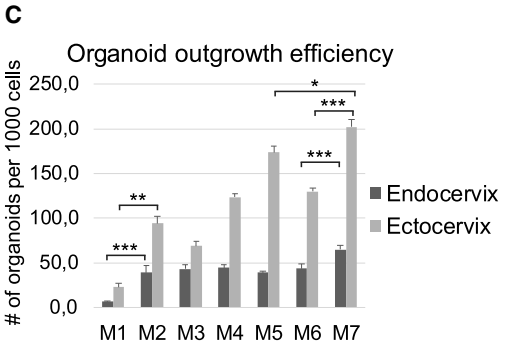

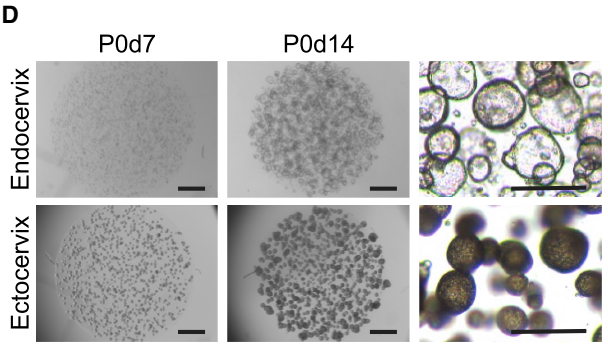

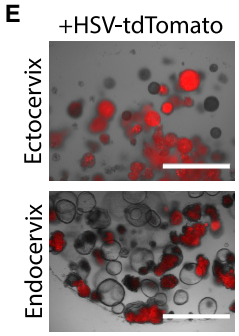

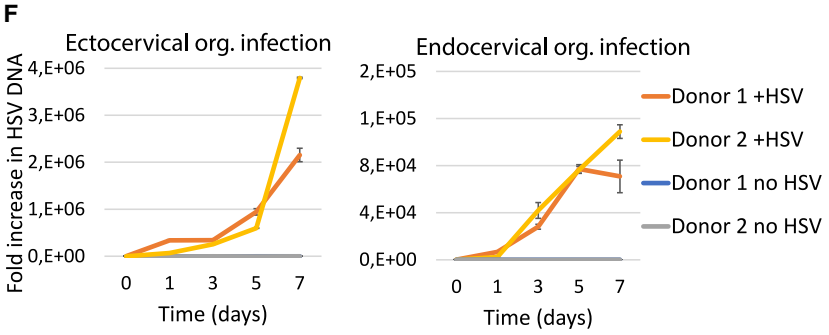

(legend on next page)

Please cite this article in press as: Lõhmussaar et al., Patient-derived organoids model cervical tissue dynamics and viral oncogenesis in cervical cancer, Cell Stem Cell (2021), https://doi.org/10.1016/j.stem.2021.03.012

To date, cervical cancer studies have relied on a limited number of cell lines and xenograft and transgenic mouse models (Larmour et al., 2015). Most of the broadly used cell lines, such as HeLa or CaSki, were established decades ago and have gone through extensive passaging. Therefore, their value for preclinical testing is limited. On the other hand, organotypic raft cultures are able to support the viral life cycle but cannot be maintained beyond 2–3 weeks (Ozbun and Patterson, 2014). Xenograft models are another approach to study the human disease. However, generation of such models for cervical cancer has been reported to be of low efficiency (Hoffmann et al., 2010). Engineered mouse models that express viral oncogenes under basal cell-specific reporters have enhanced our understanding of the role of the viral oncogenes in cervical tumorigenesis (Herber et al., 1996; Song et al., 1999). Development of novel human-based model systems is anticipated to further increase our understanding of this unique disease.

In the past decade, much progress has been made in culturing adult stem cell-based organoids, organ-like structures that self-organize in 3D culture (Huch et al., 2015; Sato et al., 2009, 2011). Following similar strategies, tumors from affected individuals can also be grown as 3D organoids (van de Wetering et al., 2015), whereas normal organoids can be driven into malignant transformation by sequential introduction of oncogenic mutations using CRISPR (Drost et al., 2015; Matano et al., 2015). Organoid technology has now been extended to a variety of gynecological tissues and tumors, including normal fallopian tubes (Kessler et al., 2015; Kopper et al., 2019), ovarian surface epithelium (Kopper et al., 2019), endometrium (Boretto et al., 2017; Turco et al., 2017), and the associated cancers (Boretto et al., 2019; Hill et al., 2018; Kopper et al., 2019). Here we report establishment of long-term human organoid cultures from healthy ecto- and endocervical tissue as well as from the associated malignancies.

RESULTS

Derivation of healthy cervical organoids and infection with HSV-1

For organoid establishment, healthy endo- and ectocervical tissues were dissected carefully from the cervical canal of women undergoing total hysterectomy. The tissues were subjected to different enzymatic treatments using collagenase (endocervix) or dispase-trypsin (ectocervix) (see STAR Methods for more details; Figure 1A). After digestion, the cells were embedded into basement membrane extract (BME) matrix and submerged in culture medium. The medium composition of both cultures was optimized for long-term expansion. Our initial basal medium (M1) contained 5 components: Noggin, nicotinamide (NIC), p38 inhibitor (p38i), B27 supplement, and Rho kinase (ROCK) inhibitor (Y27632) (Figure 1B). Noggin was selected to inhibit differentiation cues from bone morphogenic protein (BMP) signals and generally facilitates expansion of stem cells (Sato et al., 2009). Addition of NIC and p38i has been reported previously to be important for long-term organoid maintenance (Sato et al., 2011). The supplement B27 is commonly used in various organoid media to increase sphere formation efficiency. Y27632 was added to increase proliferation and prevent cell death through anoikis. In the basal medium, we observed emergence of small organoids from both lineages. However, addition of fibroblast growth factor 7 (FGF7; M2) was required to significantly increase outgrowth of the organoids (Figures 1B and 1C). Because organoid growth and maintenance were still limited under these basic conditions, we tested additional factors used in other 3D culture systems: N-acetyl cysteine (NAC), transforming growth factor β (TGF-β) inhibitor A83, forskolin (FSK), FGF10, and the canonical Wingless/Int (WNT) signaling pathway potentiator RSPO1 (Figure 1B). Stepwise addition of these growth factors improved organoid outgrowth efficiency, most notably in ectocervical cultures, for which the full medium (M7) yielded the highest organoid outgrowth number (Figures 1B and 1C). The outgrowth efficiency of endocervical organoids was found to be comparable for media M2–M6 but increased slightly in complete medium (M7) (Figures 1B and 1C). Although M7 medium was initially promising for endocervical cultures, we observed an increase in differentiated structures after 5–8 passages in culture (Figure S1A). To improve long-term maintenance, we tested supplementation of additional factors, such as epithelial growth factor (EGF), hormone β-estradiol (β-Est), and WNT activators (i.e., WNT surrogate and Chir99021 [CHIR]), which together rescued the lines from growth arrest (Figure S1A).

Under the respective optimized medium conditions, organoids from both lineages emerge within 7 days and expand fully within 14 days (Figure 1D). The endocervical organoids formed hollow cystic structures, whereas ectocervical organoids showed a dense phenotype (Figure 1D). On average, organoids could be passaged every 10–14 days, diluting the organoids 1:4 or 1:10 in endo- and ectocervical cultures, respectively. Established

Figure 1. Establishment of organoids from endo- and ectocervix

(A) Schematic overview of tissue processing. Separate biopsies from endo- and ectocervix were dissected and treated with collagenase or dispase-trypsin, respectively. The cellular fragments were seeded into basement membrane extract (BME) and cultured in the appropriate medium. Following this protocol, organoids could be derived with 82% and 93% success rates in the endo- and ectocervical lineage, respectively.

(B) Medium component withdrawal assay and representative images of cultures from both lineages under the specified conditions. Passage (P) numbers indicate the passage numbers and days (d). Scale bars, 400 μm.

(C) Number of organoids developed per 1,000 seeded cells (i.e., P0) from human endo- and ectocervix under specified culture media after 10 days in culture. Error bars represent SEM of the technical replicates (2 biological replicates with at least 2 technical replicates each, $n \geq 4$). Statistical significance was calculated by two-sided Student's t test (*$p < 0.05$, **$p < 0.01$, ***$p < 0.001$).

(D) Representative bright-field images of both cultures in their respective media over a 2-week time course. Scale bars, 2 mm (overview images) or 200 μm (magnified images).

(E) Representative images of ectocervical (top) and endocervical (bottom) organoids infected with HSV-tdTomato. Scale bars, 1 mm.

(F) Quantification of HSV-1 DNA after infection of healthy ectocervical (left) and endocervical (right) organoids derived from two different donors for both lineages. Quantitative PCR was performed with DNA obtained from organoids infected with HSV-1, and samples were harvested on days 0, 1, 3, 5, and 7 after infection. Fold increase in DNA content was calculated relative to threshold cycle (Ct) values of the uninfected control on day 0, using the delta Ct method. Data points represent the average of three technical replicates, and error bars represent the SEM.

Please cite this article in press as: Lõhmussaar et al., Patient-derived organoids model cervical tissue dynamics and viral oncogenesis in cervical cancer, Cell Stem Cell (2021), https://doi.org/10.1016/j.stem.2021.03.012

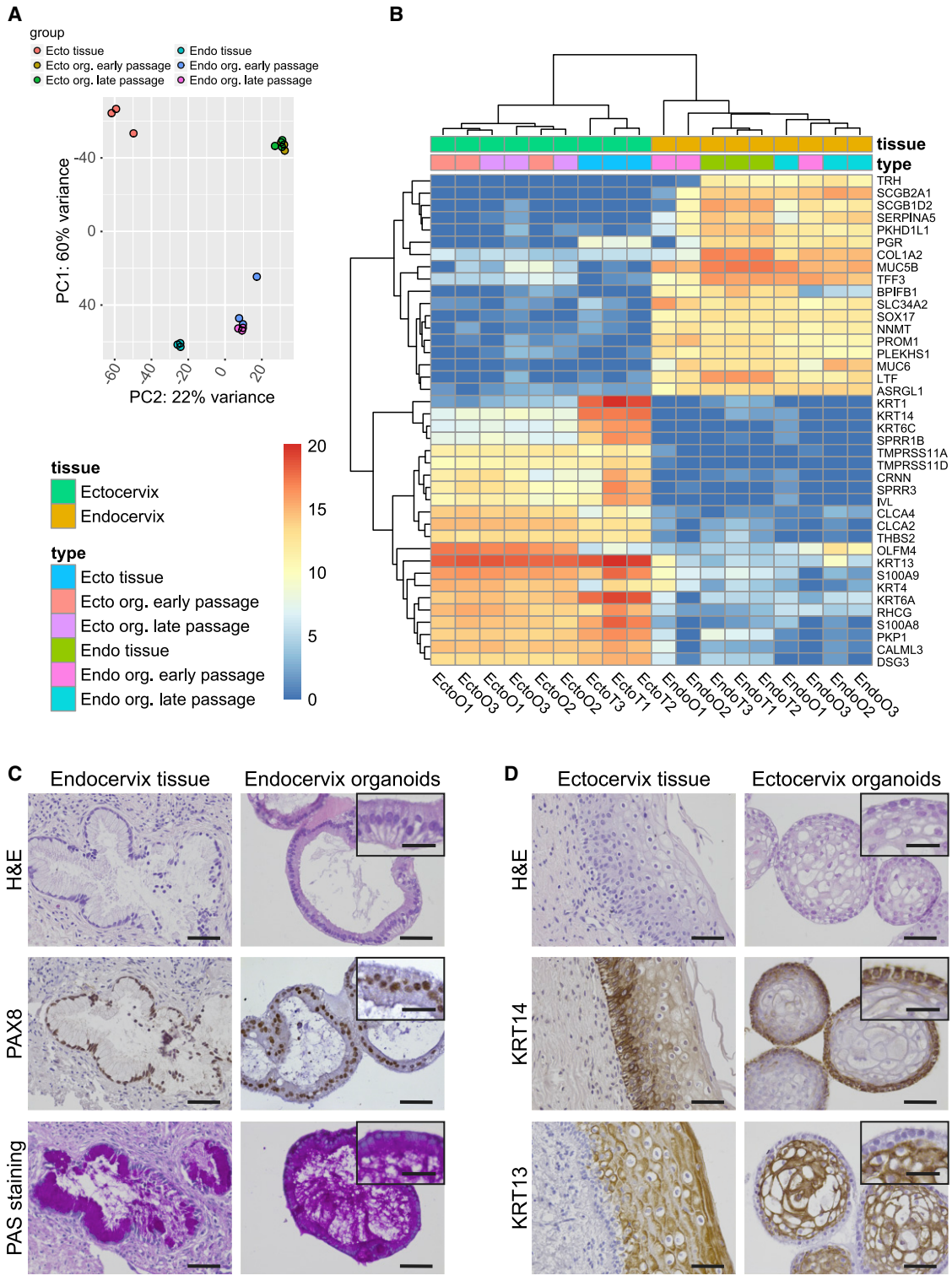

Figure 2. Marker characterization in endo- and ectocervical organoids

(A) PCA plot of RNA-seq data of normal ecto- and endocervical tissues as well as organoids in early (earlier than P5) and late (later than P10) passages (n = 3 each).

(B) Heatmap of RNA-seq data, depicting expression of the 40 most significantly differentially expressed genes between normal endo- and ectocervical tissues as well as organoids. The organoid transcriptomics profiles were analyzed in early (earlier than P5) and late passages (later than P10). Blue indicates low expression, and red indicates high expression. Differential expression was calculated as described in the DESeq2 package.

(legend continued on next page)

Please cite this article in press as: Lõhmussaar et al., Patient-derived organoids model cervical tissue dynamics and viral oncogenesis in cervical cancer, Cell Stem Cell (2021), https://doi.org/10.1016/j.stem.2021.03.012

organoid lines could be expanded long term (to date, endocervical lines more than 20 and ectocervical lines more than 30 passages), cryopreserved, and recovered successfully upon thawing. Following this protocol, healthy endo- and ectocervical organoids could be derived with a high success rate (82% and 93%, respectively). Normal organoid nomenclature and data for affected individuals for 6 thoroughly characterized healthy organoid lines are given in Table S1.

The debate regarding the presence of universal bi-potent progenitors in the human cervix that can fuel homeostasis of both types of cervical epithelium has not been settled conclusively (Chumduri, 2018; Herfs et al., 2012). Observation of WNT dependency in endocervical organoids raised the question of whether this pathway could affect transdifferentiation between the ecto- and endocervical organoid phenotype. Our data showed that exposing ectocervical organoids to WNT over a 10-day time course inhibited expansion of these organoids (Figure S1B) but did not induce expression of endocervix-specific genes such as *PAX8* and *MUC5B* (Figure S1D). Conversely, under WNT deprivation conditions, endocervical organoids collapsed, displaying a denser phenotype and growth inhibition (Figure S1B), but, similarly, this condition did not upregulate ectocervical-specific gene sets, such as *TP63*, *KRT14*, and *KRT13* (Figure S1C). These data suggested no role of the WNT pathway in transdifferentiation between the ecto- and endocervical fate. Nevertheless, our data do not exclude that cervical transdifferentiation can still be possible under other conditions.

Successful culture protocols for deriving organoids from the ecto- and endocervix can open up new doors for modeling cervical biology and diseases, including sexually transmitted infections (STIs). To show the potential of the established organoid cultures in modeling viral infection, we infected ecto- and endocervical organoid lines with tdTomato-tagged genital herpes simplex virus type 1 (HSV-1), which resulted in the emergence of a clear fluorescent signal in both lineages already 24 h after exposure, indicating successful infection (Figure 1E). Using the tdTomato-tagged virus, the viral infection could be followed visually over time by live-cell imaging in both organoid systems (Videos S1 and S2). Because this type of virus is characterized by a lytic reproduction cycle, collapse and death of the infected organoids became evident visually during the time course of exposure (Videos S1 and S2). Additionally, a substantial increase in viral DNA content was observed throughout the week after infection, confirming that the virus is able to replicate readily in both organoid types (Figure 1F).

Endo- and ectocervical organoids are miniature replicas of the originating tissues

Endo- and ectocervical epithelia display distinct morphological and transcriptional profiles. The endocervix is a glandular monolayered epithelium with pronounced secretory properties to carry out its main function: supplying mucus to lubricate the cervical canal. In contrast, stratified ectocervical architecture is maintained by basal cells that undergo proliferation and differentiation to form the dynamic multilayered squamous epithelium, which is predominantly protective in function. To better characterize the established culture systems, gene expression profiles and histological properties of both organoid lineages were analyzed and compared with their respective tissues of origin (Figures 2A–2D).

Principal-component analysis (PCA) revealed comparable gene expression patterns between the organoids and the respective tissues of origin (Figure 2A). Furthermore, both organoid lineages showed stable transcriptomes over long-term passaging (Figure 2A). Differential gene expression analysis of the RNA sequencing (RNA-seq) data separated the samples into two lineage-specific subgroups (Figure 2B). In concordance with the secretory function of endocervix, the respective tissue as well as the organoids expressed a variety of different mucins, such as *MUC5AC* and *MUC5B* (Figure 2B). In contrast, the ectocervical counterpart displayed a distinctive keratinization-associated gene signature, showing expression of a plethora of different keratins, including the basal cell marker *KRT14* and the differentiated cell marker *KRT13* but also the terminal differentiation marker *IVL*, among the most differentially expressed genes (Figure 2B). The latter implies similar stratification programs between the ectocervical tissue and organoids. Furthermore, the gene signatures were maintained between early- and late-passaged organoids, implying that the transcriptional programs of organoids remained stable during long-term passaging (Figure 2B).

This expression profile was validated by immunohistochemistry analysis (Figures 2C and 2D; Figure S2A). Standard hematoxylin and eosin (H&E) staining revealed a polarized monolayered architecture of endocervical organoids (Figure 2C), whereas a stratified multilayered phenotype was observed in ectocervical organoids (Figure 2D), both reminiscent of the respective native tissues. Under homeostatic conditions, the endocervix exhibits little capacity to proliferate, whereas the ectocervix constantly self-renews, with the latter supported by frequent division of basal cells located at the basement membrane (Figure S2A). The longevity of our organoid cultures is driven by continuous stem cell proliferation and self-renewal, which was confirmed by staining for the common proliferation marker MKI67 (Figure S2A). However, the organoids maintained an equilibrium between proliferation and maturation because mature marker expression was detected readily in both established organoid cultures.

The endocervical tissue as well as the organoids expressed the well-established secretory cell transcription marker *PAX8*, confirming their identity. Secretory products of the glandular cells were also visible in the cultures, as revealed by periodic acid-Schiff (PAS)-positive stain, confirming the functionality of the organoids (Figure 2C). Similarly, ectocervical organoids maintained a tissue-like differentiation pattern with proliferative KRT14-positive basal-like cells at the periphery of the organoids

(C) Hematoxylin and eosin (H&E) and periodic acid-Schiff (PAS) staining and positive immunostaining for PAX8 of paraffin-embedded endocervical tissue and corresponding organoids. Scale bars, 50 μm (bigger images) and 25 μm (smaller insets).
(D) H&E staining and positive immunostaining for KRT14 and KRT13 of paraffin-embedded ectocervical tissue and corresponding organoids. As seen in the staining, proliferating basal cells (KRT14 positive) are located in the periphery of the organoids, whereas the more differentiated keratinocytes (KRT13 positive) reside in the center of the organoids. Scale bars, 50 μm (bigger images) and 25 μm (smaller insets).

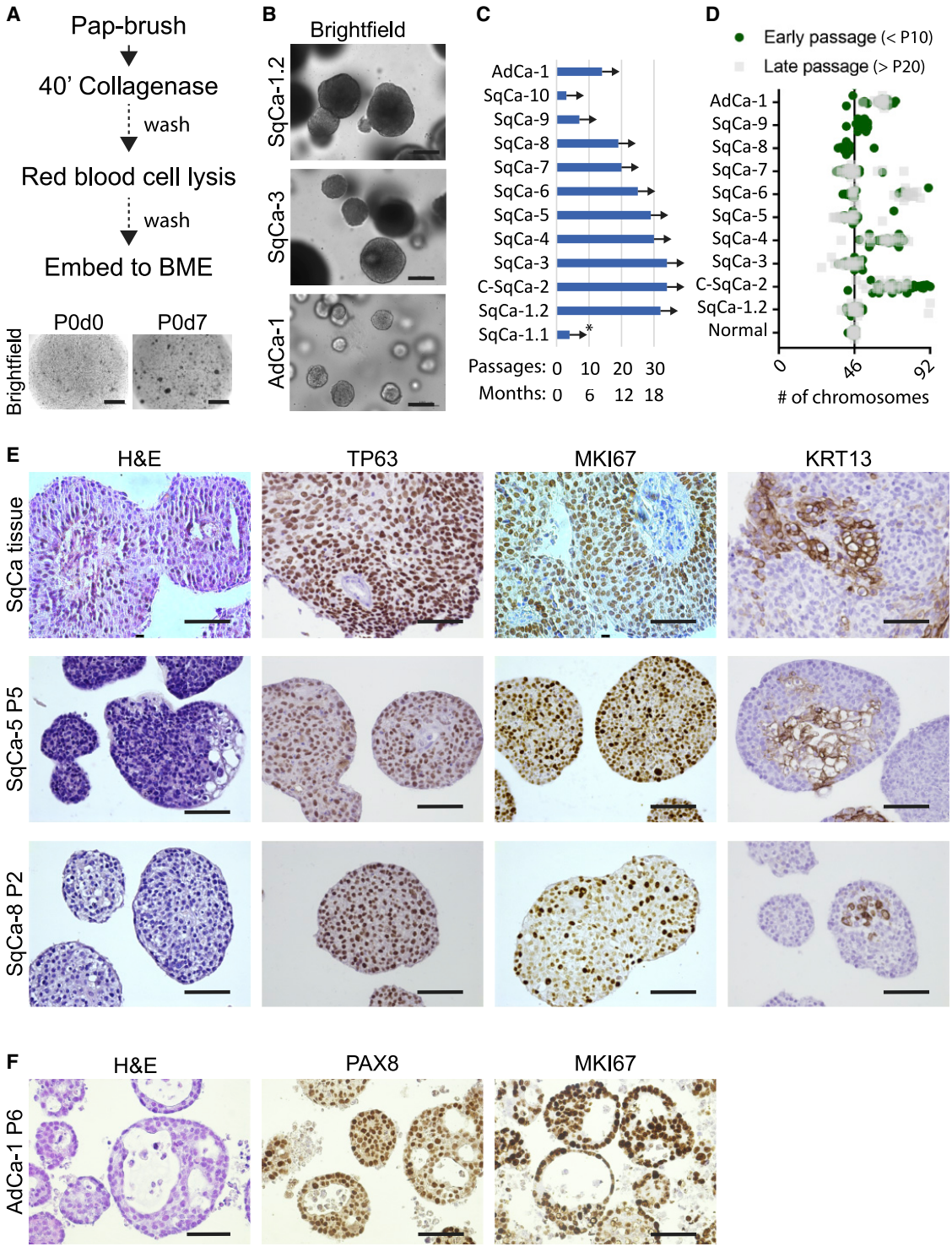

Figure 3. Establishment of cervical tumoroids derived from affected individuals

(A) Schematic of cancer tissue processing and representative images of the cultures over a 7-day time course. Scale bars, 2 mm.

(B) Representative images of tumoroid morphologies across the collected subtypes. Scale bars, 100 μm.

(C) Column bar graph depicting tumoroid maximum passage numbers up until the moment of submission. Multiple aliquots of line SqCa-1.1 (asterisk) were frozen in P4, and the culture was not continued because additional material from the same individual was received later, labeled SqCa-1.2.

(legend continued on next page)

Please cite this article in press as: Lõhmussaar et al., Patient-derived organoids model cervical tissue dynamics and viral oncogenesis in cervical cancer, Cell Stem Cell (2021), https://doi.org/10.1016/j.stem.2021.03.012

which, upon differentiation, move inward, changing in shape and size, to give rise to more differentiated KRT13-positive layers in the organoids (Figure 2D).

Further analysis of the distinct transcriptomics profile of the ectocervical organoids mainly returned keratinization-associated Gene Ontology (GO) terms (Figure S2B), whereas endocervical organoids showed enrichment in GO terms associated with cell motility and cilia (Figure S2C). In addition to secretory cells, the endocervical lining is known to also harbor ciliated cells that mediate even distribution of mucus and guidance of sperm movement along the cervical canal. The presence of ciliated cells in our endocervical organoids was further supported by high expression of ciliogenesis-related genes, including the primary ciliary transcription factor *FOXJ1* (Figure S2D), and was validated by staining for acetylated α-tubulin, which marks primary cilia (Figure S2E).

Although analysis of gene expression profiles between the organoid lines and the respective tissue samples suggested strong overlap, some degree of divergence still existed (Figure 2A). The major collective differences between healthy organoids and tissue samples could be credited to the considerably higher "replication" and "extracellular process activity" in the highly proliferative organoids and intact tissue samples, respectively (Figure S2F).

Collectively, these data revealed high similarity between the established healthy organoid lines and their respective tissues of origin in terms of histological and transcriptomics profiles, which can be stably maintained over long-term passaging.

Derivation of cervical tumoroids from Pap brush material

Introduction of the Pap test into the clinic has been instrumental in rapid early diagnosis of cervical abnormalities. As a result, the mortality rate of cervical cancer has declined significantly over the past few decades, predominantly in economically developed countries (Meggiolaro et al., 2016). Because the Pap test method is a non-invasive strategy for collecting cervical cells, we set out to test the possibility to derive cervical cancer organoids (tumoroids) from material collected via the Pap brush method. Pap tests were obtained from consenting individuals prior to surgery or treatment decision. Because the amount of tissue that can be obtained via this method is limited and enriched for blood cells, we developed a rapid digestion protocol to process the collected material, which involved initial treatment with a collagenase solution, followed by red blood cell lysis (see STAR Methods section for more details; Figure 3A). The digested material was subsequently embedded in BME and cultured in complete medium (M7), as optimized for healthy ectocervical cultures. Upon establishment, growth of tumoroids could be observed within 7 days after seeding (Figure 3A).

Because material collection via the Pap brush method is largely blinded and might yield insufficient cellular material from the tumor lesion, the success rate of tumoroid derivation using this method was found to be around 50% for SqCa (11 of 22 successful) and 25% for AdCa (1 of 4 successful). Thus, a small panel of 12 tumoroid lines was established (Table S1). Cervical cancer predominantly affects pre-menopausal women. Consistent with this, the majority of individuals were younger than 50 years of age (average age, 48; Table S1). The derived tumoroid lines displayed different morphologies, ranging from dense to cystic (Figure 3B). The tumoroids could be expanded for at least 1.5 years (>30 passages; Figure 3C) and showed varying degrees of chromosomal instability that could be maintained long term (Figures 3D). Our tumor organoid nomenclature is based on their histopathological subtype; the numbers refer to numbers of individuals. Clinical data for the individuals are presented in Table S1.

Cervical tumoroids recapitulate the disease phenotype

For the majority of the established tumoroid lines, the direct histological comparison with the matching tumor tissue of origin was not possible because of the low amount and poor integrity of the tissue collected via the Pap brush method. When the amount of collected material was sufficient, larger pieces of the scraped tissue were kept for histological, transcriptomics, or genomics analyses.

Although SqCa-derived tumoroids showed a dense morphology in culture, resembling their healthy ectocervical counterparts, histological analysis revealed a striking difference (Figure 3E). In contrast to healthy ectocervical organoids, which showed dynamic squamous differentiation features (Figure 2D), SqCa-derived tumoroid lines displayed less defined structures, as evident by loss of stratification and poor cellular polarity (Figure 3E). The tumoroids featured abundant mitotic figures and atypical, large, and hyperchromatic nuclei suggestive of neoplastic growth (Figure S3A). Additionally, tumoroids showed cytoplasmic "halos," a sign of viral infection (Figure S3A). Such histopathological features of SqCa-derived organoids could be observed in the cultures even after prolonged passaging (Figure S3B).

The abnormal features observed in the histological architecture of SqCa-derived tumoroids were also evidenced by loss of dynamic expression of stratification markers (Figure 3E). Indeed, the normally basal cell-restrictive marker TP63 was expressed abundantly throughout SqCa tumoroids, accompanied by the proliferation biomarker MKI67 (Figure 3E). In addition, tumoroids exhibited decreased expression of the differentiation marker KRT13, indicating a defect in normal squamous differentiation (Figure 3E).

In contrast to normal cystic endocervical organoids (Figure 2C), the single successfully established AdCa-derived tumoroid line showed denser structures with prominent vacuolization (Figure 3F). This morphology was retained in the AdCa-1 line even after prolonged culturing (Figure S3C). Similar to normal organoids, the AdCa-derived tumoroid line stained for PAX8, confirming its endocervical origin, and showed strong positivity for the proliferation biomarker MKI67 (Figure 3F). PAX8 and MKI67 are commonly used diagnostic markers that confirm

(D) Scatter plot presenting chromosome number distribution and mean, based on analyzed organoid metaphase spreads. In the case of "normal," the chromosome numbers were counted in three independent healthy organoid lines, and the results were merged. Karyotyping was performed in early (earlier than P10) and late (later than P20) passages when applicable ($n \geq 16$ metaphase spreads counted per line).
(E) H&E staining and immunostaining for TP63, MKI67, and KRT13 in SqCa-derived tumoroids and tumor tissue. Scale bars, 50 μm.
(F) H&E staining and immunostaining for PAX8 and MKI67 in the AdCa-derived tumoroid line. Scale bars, 50 μm.

Please cite this article in press as: Lõhmussaar et al., Patient-derived organoids model cervical tissue dynamics and viral oncogenesis in cervical cancer, Cell Stem Cell (2021), https://doi.org/10.1016/j.stem.2021.03.012

endocervical origin and determine the extent of disease (Cina et al., 1997; Danialan et al., 2013; Liang et al., 2007; Tong et al., 2011).

In addition to accumulation of histopathological features, cancer cells often lose their normal growth factor requirement upon transformation (Drost et al., 2015; Matano et al., 2015). To test whether this held true for the established cervical tumoroid lines, we performed a set of growth factor withdrawal assays that revealed distinct organoid-specific patterns in growth factor requirement (Figures S4A–S4H). Compared with healthy ectocervical organoids, in which the cells showed the highest viability in complete ectocervical medium (M7) (Figure S4A), the tumoroid lines were less dependent on the WNT pathway and mesenchymal niche factors as RSPO1 and FGF10 could be withdrawn simultaneously (medium M5) from any of the tested cultures without a significant reduction in cell viability (Figures S4B–S4H). Remarkably, in some cases, withdrawal of these factors was even beneficial for growth; three of the SqCa-derived tumoroid lines (SqCa-1.2, C-SqCa-2, and SqCa-3) performed significantly better in medium lacking RSPO1 and FGF10 compared with the full medium (Figures S4A–S4D). In contrast, although healthy endocervical organoids require factors in addition to complete ectocervical medium (M7) for optimal growth (such as activation of the EGF and WNT pathways), the AdCa-1 line showed clear independence of those factors, being able to expand equally well in the reduced media (Figures S4G and S4H). These results emphasized patient-dependent differences in tumor cell behavior captured in tumoroid models derived from affected women.

SqCa-derived tumoroids recapitulate tumor-associated gene expression patterns

To assess differences in the gene expression profiles of healthy organoids and established tumoroid lines, the samples were subjected to bulk RNA-seq analysis. PCA of healthy ecto- and endocervical as well as tumor-derived organoid lines was performed to determine the extent of similarity between the samples (Figure 4A). This analysis revealed clear transcriptomics differences between the distinct groups. The tumoroid lines formed a separate cluster, away from the normal cervix-derived organoid subgroups, but showed higher similarity to the ectocervical lineage, the anticipated origin of SqCa-derived tumoroids (Figure 4A). The AdCa-1 line displayed slight segregation from the SqCa cluster toward healthy endocervical organoids, suggesting a higher transcriptomics similarity to the endocervix than the other tumoroid lines (Figure 4A). The core gene expression profile of the tumoroid lines was highly stable over long-term passaging (Figure 4B).

Compared with purely epithelial tumoroid cultures, intact tumor tissues often possess a much higher degree of cellular complexity, containing additional non-epithelial cell types whose growth is not supported in conventional organoid cultures. Therefore, comparative transcriptomics analysis between SqCa tumor tissues and relevant organoid lines showed notable segregation (Figure S5A). However, by comparing normal ectocervical tissue samples directly with SqCa tissue samples, we were able to extract a signature gene set that specifically characterizes either of the two groups. We found 1,651 and 1,086 genes to be upregulated significantly (adjusted p [p_{adj}] < 0.05, absolute log2 fold change [log2FC] > 2) in the tumor and normal tissue subgroups, respectively (Figure S5A; Table S2). Notably, applying these gene sets to the organoid samples revealed strong tumor tissue-specific gene set enrichment only in the tumoroid subgroup (Figure S5B), whereas normal ectocervical organoids showed significant enrichment in the respective normal tissue-specific gene set (Figure S5C).

Next, differential gene expression analysis was performed between the healthy ectocervical and SqCa-derived organoid lines to determine the most differentially expressed genes between the two groups. In total, 289 genes were found to be upregulated significantly (log2FC > 2, $p_{adj} < 0.05$), whereas 814 genes were downregulated significantly (log2FC < −2, $p_{adj} < 0.05$) in SqCa-derived tumoroids compared with the healthy counterparts (Figure 4C). Extraction of the top 20 significantly upregulated genes in the tumoroid group returned a list of genes that had been associated previously with cervical cancer (Figure 4D). For instance, a host surrogate marker for viral infection, the tumor suppressor protein p16INK4a, is often used in the clinic to obtain a better indication of the viral presence in cervical tissue specimens (Lakshmi et al., 2009; Queiroz et al., 2006). As expected, *CDKN2A*, the gene that encodes for the p16INK4a protein, was seen to be overexpressed significantly in SqCa-derived tumoroids compared with the healthy counterparts (Figure 4D). This finding was confirmed by strong immunostaining for p16INK4a in the tumoroids (Figure 4E). Multiple other genes that have been associated previously with viral infection were expressed differentially in the tumoroid group. For example, the potential antiviral response inhibitor *RNF157* (Liu et al., 2018) and chromosome maintenance gene *SMC1B* (Degli Esposti et al., 2017) were found to be upregulated compared with healthy ectocervical lines (Figure 4D). In addition, among the top expressed genes, we found the tyrosine kinase receptor gene *EPHB2*, which has been shown previously to promote cervical cancer progression by inducing epithelial-to-mesenchymal transition (Gao et al., 2014), and the transcription factor *SIM2*, which has been identified recently as an independent predictive biomarker for cervical SqCa (Nakamura et al., 2017; Figure 4D). Finally, the tumoroids displayed significantly higher expression of the *LGR6*, *SYCP2*, *TCAM1P*, and *RUNX3* genes (Figure 4D). The WNT pathway regulator *LGR6* has been reported recently to be a stem cell marker in mouse skin SqCa (Huang et al., 2017), and upregulation of this gene correlates significantly with HPV status and overall survival in HPV-positive oropharyngeal SqCa (Jank et al., 2020). *SYNP2* and *TCAM1* are two testis-specific genes that are upregulated synergistically by the E6 and E7 oncogenes of HPV (Pyeon et al., 2007). *RUNX3* is involved in the TGF-β signaling pathway, which might serve as a tumor suppressor gene in cervical cancer (Li et al., 2018). Taken together, the tumoroids' gene expression profile closely reflects those observed in cervical cancer.

Tumoroids show common genomic alterations and viral integration

To analyze the mutational landscape of the tumoroids, we performed whole-exome sequencing (WES) analysis on 7 lines for which we were also able to collect DNA from a small amount of tissue prior to digestion, encompassing 6 SqCa cases and 1 AdCa case. Because we could not obtain matched normal

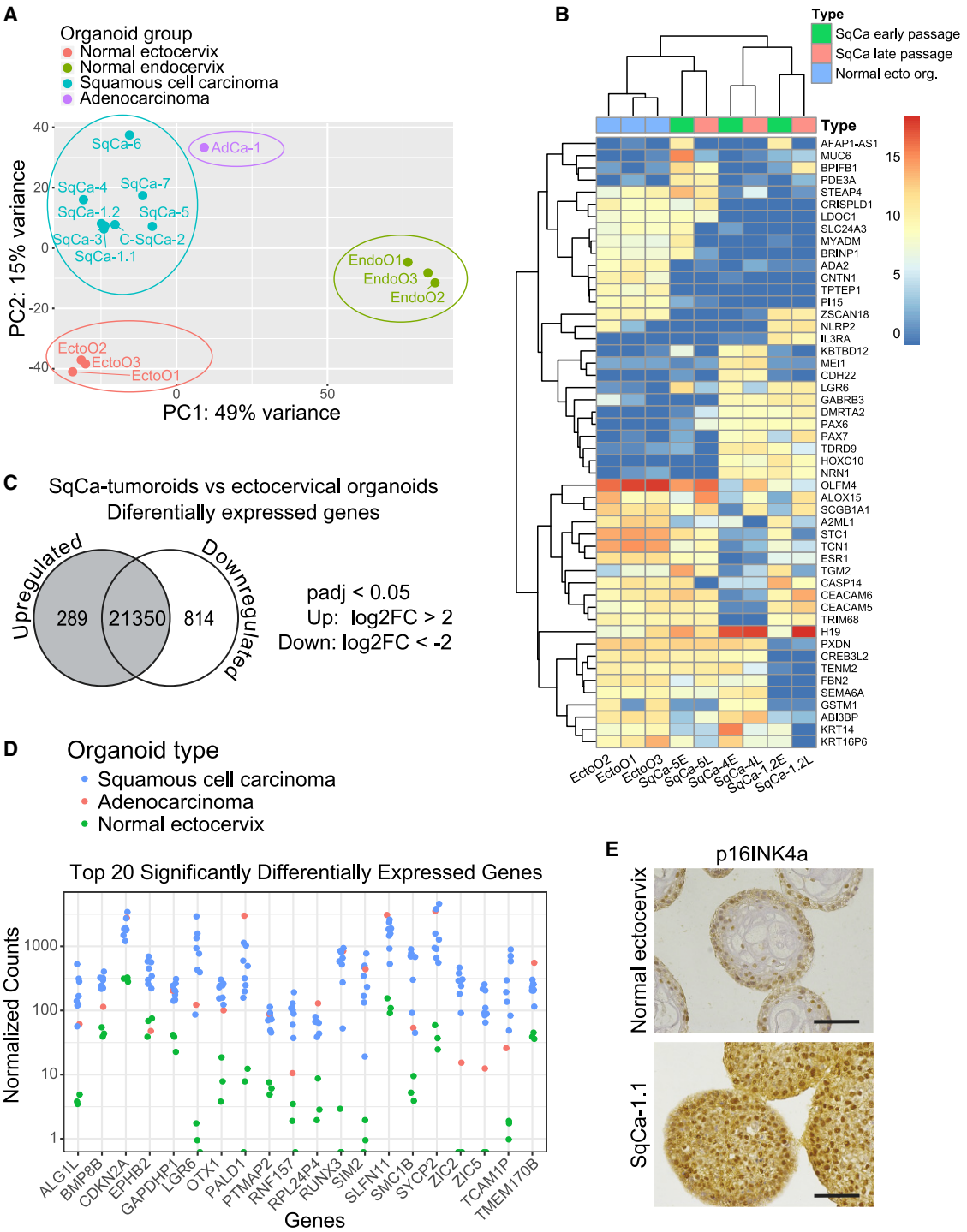

Figure 4. Gene expression profile of cervical tumoroids

(A) PCA plot of RNA-seq data of normal ecto- and endocervical organoids (n = 3 each) as well as tumoroid lines (n = 9) in early passages (earlier than P10).

(B) Heatmap of RNA-seq data depicting gene expression profiles of healthy ectocervical organoids and three SqCa-derived tumoroid lines in early (earlier than P10) and late (later than P20) passages to show the stability of the transcriptome throughout passaging. The 50 most significantly differentially expressed genes are shown. Blue indicates low expression, and red indicates high expression. Differential expression was calculated as described in the DESeq2 package.

(C) Venn diagram of differentially expressed genes in tumoroids. The results are derived from organoids in early passages (earlier than 10 passages).

(D) Plot of normalized counts depicting the top 20 most significantly upregulated genes in SqCa-derived tumoroids versus healthy ectocervical organoids. The results are derived from organoids in early passages (earlier than 10 passages).

(E) Positive immunohistochemical staining for the viral surrogate marker p16INK4a in the representative normal and SqCa-derived tumoroids. Scale bars, 50 μm.

Please cite this article in press as: Lõhmussaar et al., Patient-derived organoids model cervical tissue dynamics and viral oncogenesis in cervical cancer, Cell Stem Cell (2021), https://doi.org/10.1016/j.stem.2021.03.012

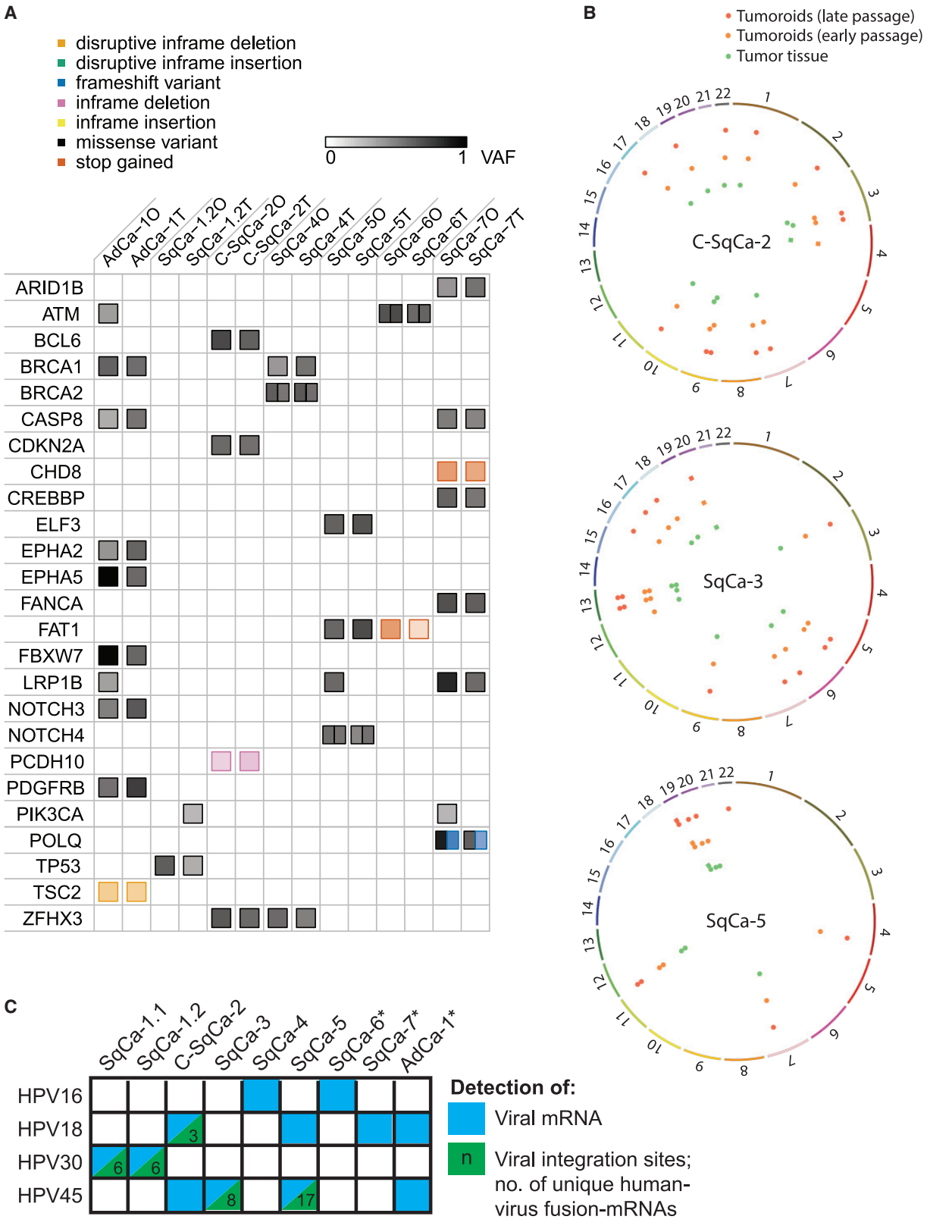

(legend on next page)

Please cite this article in press as: Lõhmussaar et al., Patient-derived organoids model cervical tissue dynamics and viral oncogenesis in cervical cancer, Cell Stem Cell (2021), https://doi.org/10.1016/j.stem.2021.03.012

tissue from individuals with tumors, it was not possible to differentiate between private germline and somatic variants. Nevertheless, for all lines, we identified unique, individual-specific mutational profiles that were largely conserved between the tumor tissues and respective tumoroids (Figure 5A; Figure S6). The mutated genes in SqCa-derived tumoroids involved common targets, such as *TP53*, *ARID1B*, *CDKN2A*, *ELF3*, and *FAT1*, and genes in the DNA repair pathway, such as *BRCA1/2*, *ATM*, and *FANCA*, showing high levels of concordance with previously identified recurrently mutated genes (Cancer Genome Atlas Research Network et al., 2017; Ojesina et al., 2014; Figure 5A). In contrast, the single AdCa-derived line harbored mutations in the two critical tumor suppressor genes, *FBXW7* and *CASP8*, which have been reported recently to be mutated in cervical cancer (Cancer Genome Atlas Research Network et al., 2017; Figure 5A). Additionally, the AdCa-1 line showed evidence of alterations in the NOTCH, TGF-β, and epinephrine signaling pathways, including *NOTCH3*, *PDGFRB* and *TSC2*, *EPHA2*, and *EPHA5*, which are all clinically actionable pathways for cancer therapy (Figure 5A). Because of the small panel size, there were only a few common targets that were shared between multiple lines, including *BRCA1*, *FAT1*, *LRP1B*, and *ZFHX3* (Figure 5A).

In the majority of cases, the tumoroids displayed higher enrichment in variant allele frequency (VAF) compared with the respective tissues, reflecting the cancer cell purity in our culture system, whereas primary tissue often contains other noncancerous cell types, such as blood cells and/or stromal components (Figure 5A). To examine the stability of the tumoroids' mutation profile for the long term, we repeated WES on 3 different late-passaged SqCa lines (Figure 5B). The analysis revealed that the majority of mutations found in the original tissue was also present in the organoids, and the core mutation profile was stably maintained over long-term passaging with a few minor losses or gains (Figure 5B). The potential driver mutations for each sample are listed in Table S3. These results indicated that the tumoroids retain genetic alterations of original tissues and faithfully represent the genomic landscape of clinical disease.

Genomic instability and somatic alterations are usually secondary by-products of cervical cancer development, which is predominantly initiated by viral oncogenesis. We were therefore interested to determine possible viral integrations and active viral transcripts in the established tumoroid lines. For this, we re-purposed our RNA-seq dataset containing information about 8 SqCa- and 1 AdCa-derived lines to search for type-specific viral transcripts and detect unique human-virus fusion mRNAs, with the latter being indicative of viral integration into the host genome. For 3 newly sequenced samples (SqCa-6, SqCa-7, and AdCa-1), viral integration analysis could not be performed because these samples were sequenced by the more economic single-end sequencing instead of paired-end sequencing. When analyzing the first 6 paired-end-sequenced SqCa tumoroids, multiple unique viral integration sites were detected in all but one line (SqCa-4), which only showed expression of high-risk HPV16 transcripts but no fusion-mRNA molecules, indicating likely episomal maintenance of the viral genome in this line (Figure 5C). In the remaining lines, several unique viral-host mRNA breakpoints were detected, indicating multiple integration sites per line (Figure 5C). In addition to integration, viral mRNA expression was detected readily in all of the analyzed tumoroids (Figure 5C). No viral transcripts or integrations were found in healthy organoid lines. Most of the tumoroid lines (7 of 9, 78%) contained viral transcripts from at least one high-risk subtype of HPV, including HPV16, HPV18, and HPV45 (Figure 5C). In three cases, active transcripts from more than one viral subtype were detected per line (HPV16/30 in SqCa-2 and HPV18/45 in the SqCa-5 and AdCa-1 lines). Interestingly, two tumoroid lines that were originally derived from the same individual at different time points (SqCa-1.1 and SqCa-1.2) only showed the presence of viral transcripts from a single, relatively poorly characterized HPV30 strain (Figure 5C). According to the International Agency for Research on Cancer (IARC) monograph on human carcinogens (International Agency for Research on Cancer, 2012), HPV30 is classified under group 2B carcinogens; i.e., among agents that are considered potentially carcinogenic. However, without sufficient evidence, the actual risk of this HPV subtype is currently unknown. Our data suggest a plausible direct carcinogenic role of HPV30.

Because viral oncogenesis is mostly facilitated by viral gene expression, we also analyzed the viral transcriptome patterns in the sequenced tumoroids. The analysis revealed that the lines predominantly express high levels of the viral oncogenes E6 and E7 (as expected), whereas most of the other viral maintenance genes were detected at lower levels (Figure S5D). Only a single line (SqCa-6) showed expression of the late viral capsid-encoding gene L1, suggesting that this line was still able to support the complete viral life cycle. The overall expression profile was maintained after long-term passaging, as shown by viral transcriptome analysis of the three independent lines that were sequenced at early and late passages: SqCa-1.2, SqCa-4, and SqCa-5 (Figure S5D). Additionally, we had sufficient material to perform viral transcriptome analysis of the originating tissues of two tumoroid lines (SqCa-1.2 and SqCa-5). The data showed similar HPV type and gene detection in matching tissues, albeit at considerably lower levels, which likely reflected the small

Figure 5. Tumoroids show common genomic alterations and viral integration

(A) Somatic mutations in relevant genes of cervical cancer. For each individual, matched tumor (T) and tumor organoid (O) pairs are displayed. VAF, variant allele frequency. A more comprehensive list of genomic alteration can be found in Figure S6. The mutation profiles are derived from organoids in early passages (earlier than P10).

(B) Circos plots of C-SqCa-2, SqCa-3, and SqCa-5 tissues (green) and respective tumoroid lines in early (earlier than P10, orange) and late (later than P20, red) passages, showing somatic mutations and their preservation in culture after long-term passaging. An individual's blood sample was used as a reference.

(C) Results from bulk RNA-seq analysis, showing the presence of subtype-specific viral transcripts (blue) in the SqCa-derived lines and a number of detected unique viral-host mRNA fusion molecules (green) that indicate viral integration sites. The results are derived from organoids in early passages (earlier than 10 passages). Viral integration could not be calculated for three lines because these lines were sequenced by single-end sequencing instead of paired-end sequencing (asterisks).

Please cite this article in press as: Lõhmussaar et al., Patient-derived organoids model cervical tissue dynamics and viral oncogenesis in cervical cancer, Cell Stem Cell (2021), https://doi.org/10.1016/j.stem.2021.03.012

amount and purity of cancer cells that can be obtained via the Pap brush method (Figure S5D).

Cervical tumoroids show differential drug responses

Besides surgical intervention, radiotherapy and its combination with chemotherapy (i.e., chemoradiation) are commonly used for treatment of cervical cancer. However, the exact benefit of combining these treatments has remained questionable in the field, and many individuals suffer from long-term adverse effects (Vale et al., 2010). Multiple studies have demonstrated recently that organoids have predictive value in cancer therapy (Ganesh et al., 2019; Ooft et al., 2019; Tiriac et al., 2018; Vlachogiannis et al., 2018; Yao et al., 2020). We therefore sought to investigate whether cervical tumoroids could be informative in such assays.

HPV oncogenes target key cell cycle control pathways, such as TP53 signaling (Huibregtse et al., 1991; Scheffner et al., 1990, 1993). Concordantly, genomic profiling of the tumoroids showed that, although only one line (i.e., SqCa-1.2) harbored a direct mutation in *TP53*, the rest of the lines showed evident aberrations in other key cell cycle genes, such as *ATM*, *ATR*, and *CDKN2A* (Figure 5A; Figure S6). We chose to first assess possible TP53 pathway defects in our tumoroid lines by using the TP53-activating compound Nutlin-3a (Figure 6A). The organoids were dissociated into single cells, suspended in complete medium (M7) containing 5% BME, and dispensed into 384-well plates. Two days after plating, the drugs were added, and cell viability was measured 5 days after supplementing the drugs. Staurosporine, a common apoptosis-inducing agent, was used as a baseline control for the assays, and the sensitivity of the lines to the drug was visualized via dose-response curves (Figures 6A and 6B). As expected, the majority of the tested SqCa tumoroids showed higher resistance to Nutlin-3a compared with the AdCa-derived and healthy lines, implicating alterations in this key oncogenic pathway in the resistant lines (Figure 6B). In accordance to the genomic data, the TP53-mutated SqCa-1.2 line was among the most resistant lines. The robustness of the drug screening assays was confirmed by a strong correlation of the average area under the dose-response curves (AUC) between biological replicates (coefficient of determination (R^2) = 0.74; Figure 6C).

Next we tested the tumoroids' sensitivity to several commonly used chemotherapy regimens, including carboplatin, cisplatin, and gemcitabine (Figures 6D–6F). These assays revealed differential drug responses of individual tumoroid lines. For example, the SqCa-3 line showed highest resistance toward treatment with the two platinum analogs (Figures 6D and 6E), whereas the SqCa-6 and SqCa-7 lines were highly sensitive to gemcitabine (Figure 6F). Because the somatic mutation analysis revealed that several lines carried mutations in DNA repair pathways, we also evaluated the effect of the most commonly used poly(ADP-ribose) polymerase (PARP) inhibitor, olaparib, which has shown good outcomes on tumors with homologous recombination (HR) repair deficiency. The results showed only little variability in the sensitivity to this drug across the tested lines (Figure 6G). Surprisingly, the two lines with *BRCA* gene aberrations (AdCa-1 and SqCa-4) were not among the most sensitive lines, indicating that the missense variants we detected in the *BRCA* genes for these lines might not induce a significant HR deficiency.

Tumoroids recapitulate characteristics of cervical tumors upon xenotransplantation

We next tested whether the cultured cervical tumoroids retained their tumorigenic potential and could be transplanted subcutaneously into immunodeficient mice. Tumoroids from 4 independent lines, SqCa-1.2, SqCa-3, SqCa-4, and AdCa-1, were injected into the right and left flanks of 4–5 immunodeficient female mice (n = 4 mice/8 locations for SqCa-1.2, n = 5 mice/10 locations for the rest). Three months following the injections, three (SqCa-1.2, SqCa-3, and AdCa-1) of four organoid lines showed 100% xenotransplantation success (Figure 7A). SqCa-4 showed a lower engraftment rate and size; small palpable tumors were observed in only 2 of 5 mice (Figure 7A). The tumors displayed line-dependent variation in size, with the AdCa line exhibiting the fastest growth (Figure 7B).

SqCa-s displayed different degrees of squamous differentiation with occasional nests of keratin (keratin pearls) (Figure 7C, asterisk). Keratinization is commonly absent in healthy ectocervical tissue but observed often in cervical tumors. Occasional superficial extensions into adjacent stromal tissue were observed, suggestive of an invasive nature (Figure 7C, black arrowhead). One of the lines that was xenografted efficiently was the HPV30-infected line SqCa-1.2, which, from the transcriptome analysis, was also shown to express high levels of the E6 and E7 oncogenes (Figure S5D), suggesting an oncogenic role of the poorly characterized HPV30 type.

AdCa displayed characteristic closely packed and irregularly shaped glands, many of which were small (Figure 7C). All tumors showed moderate proliferation capacity and stained for the surrogate marker of viral infection p16INK4a (Figure 7C).

DISCUSSION

With the emergence of adult stem cell-based organoid technology, novel 3D culture systems have been established from a variety of epithelial tissues, such as intestine (Sato et al., 2009), liver (Hu et al., 2018; Huch et al., 2015), and endometrium (Boretto et al., 2017; Turco et al., 2017). Here we show that healthy and tumor-derived cervical organoid cultures closely recapitulate their tissues of origin and are suitable for STI modeling, as evidenced by the example of the genital virus HSV-1. The precise arrangement of the layers in ectocervical organoids, where basal cells are positioned in the outermost layer, holds promise for future HPV infection assays because the stem cells are conveniently accessible for viral entry. Additionally, endocervical organoids could be used to study the development of AdCa and the biology of a number of sexually transmitted diseases, such as infection with *Chlamydia trachomatis* and *Neisseria gonorrhea*. We and others have demonstrated the feasibility of organoids to be co-cultured with microorganisms (Bartfeld et al., 2015; Driehuis et al., 2019; Heo et al., 2018; Lamers et al., 2020; Nie et al., 2018; Pleguezuelos-Manzano et al., 2020). Therefore, healthy ecto- and endocervical 3D organoid cultures may open exciting new avenues for cervical cancer and infection studies and provide new tools to learn more about the biology of the human cervical epithelium.

Obtaining access to solid tumor material often requires invasive and risk-associated tissue sampling, such as surgical biopsy collection. In this study, we describe derivation of a panel

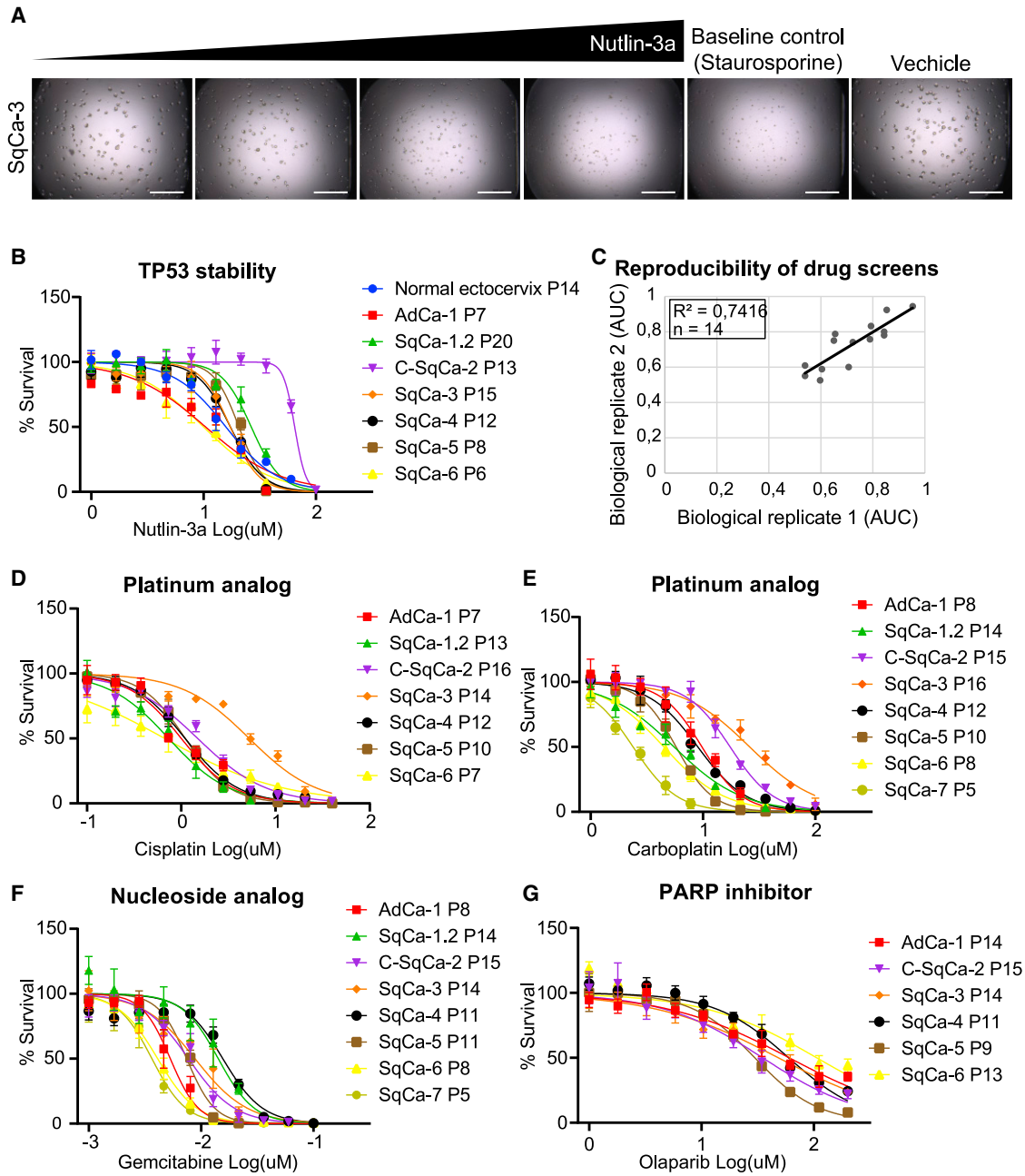

Figure 6. Cervical tumoroids show differential drug responses

(A) Representative bright-field images of Nutlin-3a-treated SqCa tumoroids. Scale bar, 500 μm.

(B) Representative dose-response curves for Nutlin-3a. SqCa-derived tumoroids are more resistant to Nutlin-3a than AdCa-derived and healthy organoids. Dots and error bars represent the mean and SEM of technical replicates, respectively (n = 3).

(C) Scatterplot of AUC values of biological replicates, displaying high correlation (R^2 = 0.74, n = 14).

(D–G) Representative dose-response curves for (D) cisplatin, (E) carboplatin, (F) gemcitabine, and (G) olaparib. Dots represent the mean of technical replicates. Error bars represent SEM of technical replicates (n = 3).

of 12 cervical tumoroid lines from tumor material collected via the Pap brush method. The observed tumoroid derivation efficiency from Pap brush material was 50% and 25% in the SqCa and AdCa subtypes, respectively, and could likely be improved upon standardization. The tumoroids can be expanded stably in the long term (>1.5 years) and show varied degrees of chromosomal instability, a hallmark of cancer. Comparative gene expression analysis of healthy ectocervical and SqCa-derived organoids revealed evident changes in the tumoroid transcriptomes. Among others, the host surrogate marker for viral infection, p16INK4a, was upregulated significantly in the tumoroid group. The tumoroids showed clear

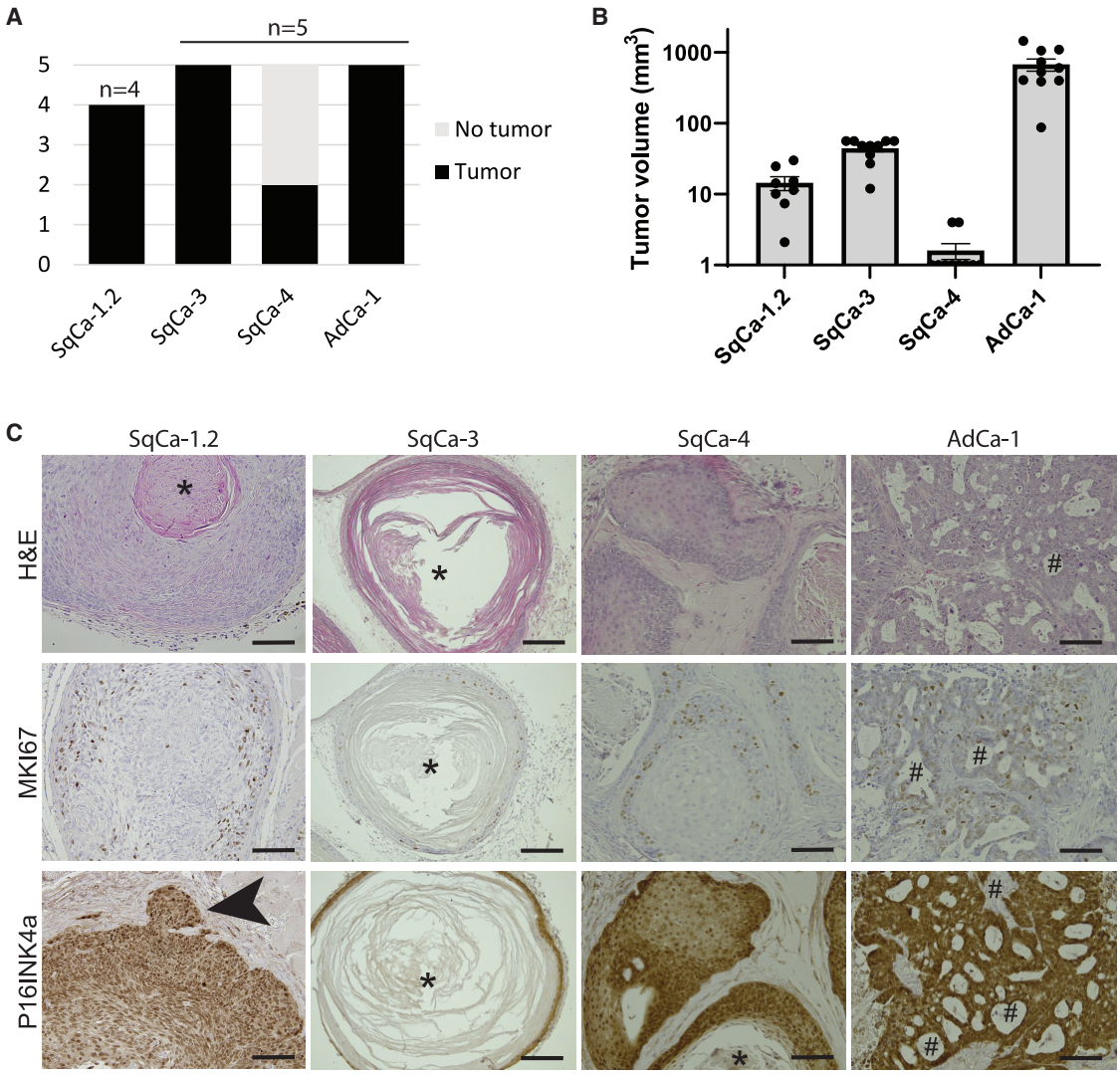

Figure 7. Xenografted cervical tumoroids recapitulate the pathohistological characteristics of cervical tumors

(A) Barplot depicting the number of mice that developed tumors after subcutaneous injections.

(B) The distribution and mean of tumor volumes derived from each line (n = 8 for SqCa-1.2, n = 10 for the rest). Error bars represent ± SEM.

(C) Representative histological overview images of tumors derived from subcutaneous injections with each tumoroid line. H&E, MKI67, and p16INK4a staining are shown. SqCa showed occasional keratin pearls (asterisks) and stromal invasion (black arrowhead), an indication of tumorigenicity. AdCa displayed closely packed glands, many of which were small (hash tags). Scale bars, 100 μm.

evidence of viral carcinogenesis: viral integration and viral oncogene expression of high-risk HPV subtypes, including HPV16, HPV18, and HPV45, were detected readily in the tested lines. Interestingly, transcripts of a single HPV30 subtype were found in two tumoroid lines sampled at different time points from the same donor. The exact carcinogenic risk of HPV30 is currently unknown. However, because the role of viral contribution to SqCa is well established, and because we observed high viral oncogene expression, our data encourage further research of HPV30 and its potential direct role in cervical carcinogenesis.

As a rewarding outcome of prevention measures, cervical cancer incidence has declined drastically over the years (Yang et al., 2018). Consequently, clinical trials for optimizing treatment regimens have become increasingly challenging. Therefore, new platforms that enable prediction of an individuals' response in a more personalized fashion are needed. We performed drug screening assays on a panel of cervical cancer tumoroids that revealed differential responses to the tested common chemotherapy regimens. Although encouraging, observational trials will be required to determine the predictive value of tumoroid drug screening in a precision medicine setting.

Limitations of study

Although the current work introduces an organoid-based platform for studying the human cervix, it only explores the tip of the iceberg of exciting applications these cultures could provide to model this organ in health and disease. Given the long-term

expansion and spontaneous squamous stratification of ectocervical organoids, it is very inviting to imagine the powerful way in which these models could advance our knowledge of natural HPV infection and the resulting cervical cancers. Additionally, it is very important to increase the size of the small tumoroid biobank reported here to capture the entire disease heterogeneity and work toward novel treatment strategies.

STAR★METHODS

Detailed methods are provided in the online version of this paper and include the following:

- KEY RESOURCES TABLE
- RESOURCE AVAILABILITY
  - Lead contact
  - Materials availability
  - Data and code availaility
- EXPERIMENTAL MODEL AND SUBJECT DETAILS
  - Human material for organoid culture
  - Mice
- METHOD DETAILS
  - Healthy endo- and ectocervical organoid culture
  - Tumor-derived organoid (tumoroid) culture
  - Organoid formation efficiency assay
  - HSV-1 infection and quantification experiments
  - Karyotyping
  - Immunohistochemistry
  - RNA isolation, cDNA preparation and RT-qPCR
  - Bulk RNA-seq analysis
  - Viral subtype detection and integration analysis
  - Viral transcriptome analysis
  - DNA extraction and whole-exome sequencing analysis
  - *In vitro* drug screen
  - *In vivo* xenotransplantation assays
- QUANTIFICATION AND STATISTICAL ANALYSIS

SUPPLEMENTAL INFORMATION

Supplemental information can be found online at https://doi.org/10.1016/j.stem.2021.03.012.

ACKNOWLEDGMENTS

We thank A. Brousali, A. Snelting, K. Oosting, and C. Hulsbergen-Veelken of the Utrecht Platform for Organoid Technology (U-PORT) as well as C. de Witte and E. Stello for patient inclusion and tissue acquisition. We thank Anko de Graaff from the Hubrecht Imaging Centre (HIC) and the Utrecht Sequencing Facility (USEQ) for the library preparations, sequencing, and data analysis of cervical organoids. This work is part of the Oncode Institute, which is partly financed by the Dutch Cancer Society and was funded by the gravitation program CancerGenomiCs.nl from the Netherlands Organisation for Scientific Research (NWO) and a grant from the Gieskes-Strijbis Foundation (1816199). R.v.B. was supported by a VIDI grant from the NWO (016.Vidi.171.023).

AUTHOR CONTRIBUTIONS

Conceptualization, K.L. and H.C.; methodology, K.L. and H.C.; software, K.L., R.O., and J.E.V.-I.; formal analysis and data interpretation, K.L., R.O., J.E.V.-I., M.H.H.S., H.W., T.G.N.J., and R.v.B.; investigation, K.L., R.O., J.E.V.-I., M.H.H.S., and H.W.; technical support, J.K. and H.B.; transplantations, N.P. and M.v.d.V.; resources, O.W.K., R.P.Z., and S.V.; data curation, K.L.

DECLARATION OF INTERESTS

H.C. is an inventor on several patents involving adult stem cell-based organoid technology. His full declaration is given at https://www.uu.nl/staff/JCClevers/.

Received: June 2, 2020
Revised: January 8, 2021
Accepted: March 15, 2021
Published: April 13, 2021

REFERENCES

Androphy, E.J., Hubbert, N.L., Schiller, J.T., and Lowy, D.R. (1987). Identification of the HPV-16 E6 protein from transformed mouse cells and human cervical carcinoma cell lines. EMBO J. *6*, 989–992.

Banks, L., Spence, P., Androphy, E., Hubbert, N., Matlashewski, G., Murray, A., and Crawford, L. (1987). Identification of human papillomavirus type 18 E6 polypeptide in cells derived from human cervical carcinomas. J. Gen. Virol. *68*, 1351–1359.

Bartfeld, S., Bayram, T., van de Wetering, M., Huch, M., Begthel, H., Kujala, P., Vries, R., Peters, P.J., and Clevers, H. (2015). In vitro expansion of human gastric epithelial stem cells and their responses to bacterial infection. Gastroenterology *148*, 126–136.e6.

Boretto, M., Cox, B., Noben, M., Hendriks, N., Fassbender, A., Roose, H., Amant, F., Timmerman, D., Tomassetti, C., Vanhie, A., et al. (2017). Development of organoids from mouse and human endometrium showing endometrial epithelium physiology and long-term expandability. Development *144*, 1775–1786.

Boretto, M., Maenhoudt, N., Luo, X., Hennes, A., Boeckx, B., Bui, B., Heremans, R., Perneel, L., Kobayashi, H., Van Zundert, I., et al. (2019). Patient-derived organoids from endometrial disease capture clinical heterogeneity and are amenable to drug screening. Nat. Cell Biol. *21*, 1041–1051.

Bosch, F.X., Lorincz, A., Muñoz, N., Meijer, C.J., and Shah, K.V. (2002). The causal relation between human papillomavirus and cervical cancer. J. Clin. Pathol. *55*, 244–265.

Cancer Genome Atlas Research Network; Albert Einstein College of Medicine; Analytical Biological Services; Barretos Cancer Hospital; Baylor College of Medicine; Beckman Research Institute of City of Hope; Buck Institute for Research on Aging; Canada's Michael Smith Genome Sciences Centre; Harvard Medical School; Helen F. Graham Cancer Center & Research Institute at Christiana Care Health Services (2017). Integrated genomic and molecular characterization of cervical cancer. Nature *543*, 378–384.

Chen, Y., Yao, H., Thompson, E.J., Tannir, N.M., Weinstein, J.N., and Su, X. (2013). VirusSeq: software to identify viruses and their integration sites using next-generation sequencing of human cancer tissue. Bioinformatics *29*, 266–267.

Chumduri, C.G., K, R., Berger, H., Koster, S., Brinkmann, V., Klemm, U., Mollenkopf, H.-J., Herbst, H., Mangler, M., and Meyer, T.F. (2018). Transition of Wnt signaling microenvironment delineates the squamo-columnar junction and emergence of squamous metaplasia of the cervix. Nat. Cell Biol. *23*, 184–197.

Cina, S.J., Richardson, M.S., Austin, R.M., and Kurman, R.J. (1997). Immunohistochemical staining for Ki-67 antigen, carcinoembryonic antigen, and p53 in the differential diagnosis of glandular lesions of the cervix. Mod. Pathol. *10*, 176–180.

Cohen, P.A., Jhingran, A., Oaknin, A., and Denny, L. (2019). Cervical cancer. Lancet *393*, 169–182.

Danialan, R., Assaad, M., Burghardt, J., Newcomb, P., Cartun, R.W., and Mandavilli, S. (2013). The utility of PAX8 and IMP3 immunohistochemical stains in the differential diagnosis of benign, premalignant, and malignant endocervical glandular lesions. Gynecol. Oncol. *130*, 383–388.

Degli Esposti, D., Sklias, A., Lima, S.C., Beghelli-de la Forest Divonne, S., Cahais, V., Fernandez-Jimenez, N., Cros, M.P., Ecsedi, S., Cuenin, C., Bouaoun, L., et al. (2017). Unique DNA methylation signature in HPV-positive head and neck squamous cell carcinomas. Genome Med. *9*, 33.

DePristo, M.A., Banks, E., Poplin, R., Garimella, K.V., Maguire, J.R., Hartl, C., Philippakis, A.A., del Angel, G., Rivas, M.A., Hanna, M., et al. (2011). A framework for variation discovery and genotyping using next-generation DNA sequencing data. Nat Genet. *43*, 491–498.

Driehuis, E., Kolders, S., Spelier, S., Lõhmussaar, K., Willems, S.M., Devriese, L.A., de Bree, R., de Ruiter, E.J., Korving, J., Begthel, H., et al. (2019). Oral Mucosal Organoids as a Potential Platform for Personalized Cancer Therapy. Cancer Discov. *9*, 852–871.

Drost, J., van Jaarsveld, R.H., Ponsioen, B., Zimberlin, C., van Boxtel, R., Buijs, A., Sachs, N., Overmeer, R.M., Offerhaus, G.J., Begthel, H., et al. (2015). Sequential cancer mutations in cultured human intestinal stem cells. Nature *521*, 43–47.

Fan, T., Li, X., Li, Y., Zhi, Y., Rong, S., Cheng, G., and Zhang, X. (2018). An improved method for primary culture of normal cervical epithelial cells and establishment of cell model in vitro with HPV-16 E6 gene by lentivirus. J. Cell. Physiol. *233*, 2773–2780.

Ganesh, K., Wu, C., O'Rourke, K.P., Szeglin, B.C., Zheng, Y., Sauvé, C.G., Adileh, M., Wasserman, I., Marco, M.R., Kim, A.S., et al. (2019). A rectal cancer organoid platform to study individual responses to chemoradiation. Nat. Med. *25*, 1607–1614.

Gao, Q., Liu, W., Cai, J., Li, M., Gao, Y., Lin, W., and Li, Z. (2014). EphB2 promotes cervical cancer progression by inducing epithelial-mesenchymal transition. Hum. Pathol. *45*, 372–381.

Heo, I., Dutta, D., Schaefer, D.A., Iakobachvili, N., Artegiani, B., Sachs, N., Boonekamp, K.E., Bowden, G., Hendrickx, A.P.A., Willems, R.J.L., et al. (2018). Modelling Cryptosporidium infection in human small intestinal and lung organoids. Nat. Microbiol. *3*, 814–823.

Herber, R., Liem, A., Pitot, H., and Lambert, P.F. (1996). Squamous epithelial hyperplasia and carcinoma in mice transgenic for the human papillomavirus type 16 E7 oncogene. J. Virol. *70*, 1873–1881.

Herfs, M., Yamamoto, Y., Laury, A., Wang, X., Nucci, M.R., McLaughlin-Drubin, M.E., Münger, K., Feldman, S., McKeon, F.D., Xian, W., and Crum, C.P. (2012). A discrete population of squamocolumnar junction cells implicated in the pathogenesis of cervical cancer. Proc. Natl. Acad. Sci. USA *109*, 10516–10521.

Hill, S.J., Decker, B., Roberts, E.A., Horowitz, N.S., Muto, M.G., Worley, M.J., Jr., Feltmate, C.M., Nucci, M.R., Swisher, E.M., Nguyen, H., et al. (2018). Prediction of DNA Repair Inhibitor Response in Short-Term Patient-Derived Ovarian Cancer Organoids. Cancer Discov. *8*, 1404–1421.

Hoffmann, C., Bachran, C., Stanke, J., Elezkurtaj, S., Kaufmann, A.M., Fuchs, H., Loddenkemper, C., Schneider, A., and Cichon, G. (2010). Creation and characterization of a xenograft model for human cervical cancer. Gynecol. Oncol. *118*, 76–80.

Horn, J., Denecke, A., Luyten, A., Rothe, B., Reinecke-Lüthge, A., Mikolajczyk, R., and Petry, K.U. (2019). Reduction of cervical cancer incidence within a primary HPV screening pilot project (WOLPHSCREEN) in Wolfsburg, Germany. Br. J. Cancer *120*, 1015–1022.

Hu, H., Gehart, H., Artegiani, B., Lopez-Iglesias, C., Dekkers, F., Basak, O., van Es, J., Chuva de Sousa Lopes, S.M., Begthel, H., Korving, J., et al. (2018). Long-Term Expansion of Functional Mouse and Human Hepatocytes as 3D Organoids. Cell *175*, 1591–1606.e19.

Huang, P.Y., Kandyba, E., Jabouille, A., Sjolund, J., Kumar, A., Halliwill, K., McCreery, M., DelRosario, R., Kang, H.C., Wong, C.E., et al. (2017). Lgr6 is a stem cell marker in mouse skin squamous cell carcinoma. Nat. Genet. *49*, 1624–1632.

Huch, M., Gehart, H., van Boxtel, R., Hamer, K., Blokzijl, F., Verstegen, M.M., Ellis, E., van Wenum, M., Fuchs, S.A., de Ligt, J., et al. (2015). Long-term culture of genome-stable bipotent stem cells from adult human liver. Cell *160*, 299–312.

Huibregtse, J.M., Scheffner, M., and Howley, P.M. (1991). A cellular protein mediates association of p53 with the E6 oncoprotein of human papillomavirus types 16 or 18. EMBO J. *10*, 4129–4135.

International Agency for Research on Cancer (2012). A review of human carcinogens. https://publications.iarc.fr/Book-And-Report-Series/Iarc-Monographs-On-The-Identification-Of-Carcinogenic-Hazards-To-Humans/Review-Of-Human-Carcinogens-Package-Of-6-Volumes-A-B-C-D-E-F-2012.

Isidean, S.D., Mayrand, M.H., Ramanakumar, A.V., Gilbert, L., Reid, S.L., Rodrigues, I., Ferenczy, A., Ratnam, S., Coutlée, F., and Franco, E.L.; CCCaST Study Group (2016). Human papillomavirus testing versus cytology in primary cervical cancer screening: End-of-study and extended follow-up results from the Canadian cervical cancer screening trial. Int. J. Cancer *139*, 2456–2466.

Jank, B.J., Kadletz, L., Dunkler, D., Haas, M., Schnoell, J., Kenner, L., and Heiduschka, G. (2020). Epithelial stem cell marker LGR6 expression identifies a low-risk subgroup in human papillomavirus positive oropharyngeal squamous cell carcinoma. Oral Oncol. *105*, 104657.

Kajitani, N., Satsuka, A., Kawate, A., and Sakai, H. (2012). Productive Lifecycle of Human Papillomaviruses that Depends Upon Squamous Epithelial Differentiation. Front. Microbiol. *3*, 152.

Kessler, M., Hoffmann, K., Brinkmann, V., Thieck, O., Jackisch, S., Toelle, B., Berger, H., Mollenkopf, H.J., Mangler, M., Sehouli, J., et al. (2015). The Notch and Wnt pathways regulate stemness and differentiation in human fallopian tube organoids. Nat. Commun. *6*, 8989.

Kopper, O., de Witte, C.J., Lõhmussaar, K., Valle-Inclan, J.E., Hami, N., Kester, L., Balgobind, A.V., Korving, J., Proost, N., Begthel, H., et al. (2019). An organoid platform for ovarian cancer captures intra- and interpatient heterogeneity. Nat. Med. *25*, 838–849.

Lakshmi, S., Rema, P., and Somanathan, T. (2009). p16ink4a is a surrogate marker for high-risk and malignant cervical lesions in the presence of human papillomavirus. Pathobiology *76*, 141–148.

Lamers, M.M., Beumer, J., van der Vaart, J., Knoops, K., Puschhof, J., Breugem, T.I., Ravelli, R.B.G., Paul van Schayck, J., Mykytyn, A.Z., Duimel, H.Q., et al. (2020). SARS-CoV-2 productively infects human gut enterocytes. Science *369*, 50–54.

Langmead, B., and Salzberg, S.L. (2012). Fast gapped-read alignment with Bowtie 2. Nat. Methods *9*, 357–359.

Larmour, L.I., Jobling, T.W., and Gargett, C.E. (2015). A Review of Current Animal Models for the Study of Cervical Dysplasia and Cervical Carcinoma. Int. J. Gynecol. Cancer *25*, 1345–1352.

Li, H., and Durbin, R. (2009). Fast and accurate short read alignment with Burrows-Wheeler transform. Bioinformatics *25*, 1754–1760.

Li, Z., Fan, P., Deng, M., and Zeng, C. (2018). The roles of RUNX3 in cervical cancer cells *in vitro*. Oncol. Lett. *15*, 8729–8734.

Liang, J., Mittal, K.R., Wei, J.J., Yee, H., Chiriboga, L., and Shukla, P. (2007). Utility of p16INK4a, CEA, Ki67, P53 and ER/PR in the differential diagnosis of benign, premalignant, and malignant glandular lesions of the uterine cervix and their relationship with Silverberg scoring system for endocervical glandular lesions. Int. J. Gynecol. Pathol. *26*, 71–75.

Liu, S., Jiang, M., Wang, W., Liu, W., Song, X., Ma, Z., Zhang, S., Liu, L., Liu, Y., and Cao, X. (2018). Nuclear RNF2 inhibits interferon function by promoting K33-linked STAT1 disassociation from DNA. Nat. Immunol. *19*, 41–52.

Love, M.I., Huber, W., and Anders, S. (2014). Moderated estimation of fold change and dispersion for RNA-seq data with DESeq2. Genome Biol. *15*, 550.

Matano, M., Date, S., Shimokawa, M., Takano, A., Fujii, M., Ohta, Y., Watanabe, T., Kanai, T., and Sato, T. (2015). Modeling colorectal cancer using CRISPR-Cas9-mediated engineering of human intestinal organoids. Nat. Med. *21*, 256–262.

Meggiolaro, A., Unim, B., Semyonov, L., Miccoli, S., Maffongelli, E., and La Torre, G. (2016). The role of Pap test screening against cervical cancer: a systematic review and meta-analysis. Clin. Ter. *167*, 124–139.

Nakamura, K., Komatsu, M., Chiwaki, F., Takeda, T., Kobayashi, Y., Banno, K., Aoki, D., Yoshida, T., and Sasaki, H. (2017). SIM2l attenuates resistance to hypoxia and tumor growth by transcriptional suppression of HIF1A in uterine cervical squamous cell carcinoma. Sci. Rep. *7*, 14574.

Nguyen, N.D., Deshpande, V., Luebeck, J., Mischel, P.S., and Bafna, V. (2018). ViFi: accurate detection of viral integration and mRNA fusion reveals indiscriminate and unregulated transcription in proximal genomic regions in cervical cancer. Nucleic Acids Res. *46*, 3309–3325.

Nie, Y.Z., Zheng, Y.W., Miyakawa, K., Murata, S., Zhang, R.R., Sekine, K., Ueno, Y., Takebe, T., Wakita, T., Ryo, A., and Taniguchi, H. (2018). Recapitulation of hepatitis B virus-host interactions in liver organoids from human induced pluripotent stem cells. EBioMedicine *35*, 114–123.

Ojesina, A.I., Lichtenstein, L., Freeman, S.S., Pedamallu, C.S., Imaz-Rosshandler, I., Pugh, T.J., Cherniack, A.D., Ambrogio, L., Cibulskis, K., Bertelsen, B., et al. (2014). Landscape of genomic alterations in cervical carcinomas. Nature *506*, 371–375.

Ooft, S.N., Weeber, F., Dijkstra, K.K., McLean, C.M., Kaing, S., van Werkhoven, E., Schipper, L., Hoes, L., Vis, D.J., van de Haar, J., et al. (2019). Patient-derived organoids can predict response to chemotherapy in metastatic colorectal cancer patients. Sci. Transl. Med. *11*, eaay2574.

Ozbun, M.A., and Patterson, N.A. (2014). Using organotypic (raft) epithelial tissue cultures for the biosynthesis and isolation of infectious human papillomaviruses. Curr. Protoc. Microbiol. *34*, 14B.3.1-18.

Phelps, W.C., Yee, C.L., Münger, K., and Howley, P.M. (1988). The human papillomavirus type 16 E7 gene encodes transactivation and transformation functions similar to those of adenovirus E1A. Cell *53*, 539–547.

Pleguezuelos-Manzano, C., Puschhof, J., Rosendahl Huber, A., van Hoeck, A., Wood, H.M., Nomburg, J., Gurjao, C., Manders, F., Dalmasso, G., Stege, P.B., et al.; Genomics England Research Consortium (2020). Mutational signature in colorectal cancer caused by genotoxic pks^{+} E. coli. Nature *580*, 269–273.

Pyeon, D., Newton, M.A., Lambert, P.F., den Boon, J.A., Sengupta, S., Marsit, C.J., Woodworth, C.D., Connor, J.P., Haugen, T.H., Smith, E.M., et al. (2007). Fundamental differences in cell cycle deregulation in human papillomavirus-positive and human papillomavirus-negative head/neck and cervical cancers. Cancer Res. *67*, 4605–4619.

Queiroz, C., Silva, T.C., Alves, V.A., Villa, L.L., Costa, M.C., Travassos, A.G., Filho, J.B., Studart, E., Cheto, T., and de Freitas, L.A. (2006). P16(INK4a) expression as a potential prognostic marker in cervical pre-neoplastic and neoplastic lesions. Pathol. Res. Pract. *202*, 77–83.

Randall, T.C., and Ghebre, R. (2016). Challenges in Prevention and Care Delivery for Women with Cervical Cancer in Sub-Saharan Africa. Front. Oncol. *6*, 160.

Ronco, G., Dillner, J., Elfström, K.M., Tunesi, S., Snijders, P.J., Arbyn, M., Kitchener, H., Segnan, N., Gilham, C., Giorgi-Rossi, P., et al.; International HPV screening working group (2014). Efficacy of HPV-based screening for prevention of invasive cervical cancer: follow-up of four European randomised controlled trials. Lancet *383*, 524–532.

Sato, T., Vries, R.G., Snippert, H.J., van de Wetering, M., Barker, N., Stange, D.E., van Es, J.H., Abo, A., Kujala, P., Peters, P.J., and Clevers, H. (2009). Single Lgr5 stem cells build crypt-villus structures in vitro without a mesenchymal niche. Nature *459*, 262–265.

Sato, T., Stange, D.E., Ferrante, M., Vries, R.G., Van Es, J.H., Van den Brink, S., Van Houdt, W.J., Pronk, A., Van Gorp, J., Siersema, P.D., and Clevers, H. (2011). Long-term expansion of epithelial organoids from human colon, adenoma, adenocarcinoma, and Barrett's epithelium. Gastroenterology *141*, 1762–1772.

Scheffner, M., Werness, B.A., Huibregtse, J.M., Levine, A.J., and Howley, P.M. (1990). The E6 oncoprotein encoded by human papillomavirus types 16 and 18 promotes the degradation of p53. Cell *63*, 1129–1136.

Scheffner, M., Huibregtse, J.M., Vierstra, R.D., and Howley, P.M. (1993). The HPV-16 E6 and E6-AP complex functions as a ubiquitin-protein ligase in the ubiquitination of p53. Cell *75*, 495–505.

Schwarz, E., Freese, U.K., Gissmann, L., Mayer, W., Roggenbuck, B., Stremlau, A., and zur Hausen, H. (1985). Structure and transcription of human papillomavirus sequences in cervical carcinoma cells. Nature *314*, 111–114.

Shrestha, A.D., Neupane, D., Vedsted, P., and Kallestrup, P. (2018). Cervical Cancer Prevalence, Incidence and Mortality in Low and Middle Income Countries: A Systematic Review. Asian Pac. J. Cancer Prev. *19*, 319–324.

Song, S., Pitot, H.C., and Lambert, P.F. (1999). The human papillomavirus type 16 E6 gene alone is sufficient to induce carcinomas in transgenic animals. J. Virol. *73*, 5887–5893.

Tarasov, A., Vilella, A.J., Cuppen, E., Nijman, I.J., and Prins, P. (2015). Sambamba: fast processing of NGS alignment formats. Bioinformatics *31*, 2032–2034.

Tiriac, H., Belleau, P., Engle, D.D., Plenker, D., Deschênes, A., Somerville, T.D.D., Froeling, F.E.M., Burkhart, R.A., Denroche, R.E., Jang, G.H., et al. (2018). Organoid Profiling Identifies Common Responders to Chemotherapy in Pancreatic Cancer. Cancer Discov. *8*, 1112–1129.

Tong, G.X., Devaraj, K., Hamele-Bena, D., Yu, W.M., Turk, A., Chen, X., Wright, J.D., and Greenebaum, E. (2011). Pax8: a marker for carcinoma of Müllerian origin in serous effusions. Diagn. Cytopathol. *39*, 567–574.

Turco, M.Y., Gardner, L., Hughes, J., Cindrova-Davies, T., Gomez, M.J., Farrell, L., Hollinshead, M., Marsh, S.G.E., Brosens, J.J., Critchley, H.O., et al. (2017). Long-term, hormone-responsive organoid cultures of human endometrium in a chemically defined medium. Nat. Cell Biol. *19*, 568–577.

Vale, C., Nightingale, A., Spera, N., Whelan, A., Hanley, B., and Tierney, J.F. (2010). Late complications from chemoradiotherapy for cervical cancer: reflections from cervical cancer survivors 10 years after the national cancer institute alert. Clin. Oncol. (R. Coll. Radiol.) *22*, 588–589.

van de Wetering, M., Francies, H.E., Francis, J.M., Bounova, G., Iorio, F., Pronk, A., van Houdt, W., van Gorp, J., Taylor-Weiner, A., Kester, L., et al. (2015). Prospective derivation of a living organoid biobank of colorectal cancer patients. Cell *161*, 933–945.

Van Doorslaer, K., Li, Z., Xirasagar, S., Maes, P., Kaminsky, D., Liou, D., Sun, Q., Kaur, R., Huyen, Y., and McBride, A.A. (2017). The Papillomavirus Episteme: a major update to the papillomavirus sequence database. Nucleic Acids Res. *45* (D1), D499–D506.

Vlachogiannis, G., Hedayat, S., Vatsiou, A., Jamin, Y., Fernández-Mateos, J., Khan, K., Lampis, A., Eason, K., Huntingford, I., Burke, R., et al. (2018). Patient-derived organoids model treatment response of metastatic gastrointestinal cancers. Science *359*, 920–926.

Yang, D.X., Soulos, P.R., Davis, B., Gross, C.P., and Yu, J.B. (2018). Impact of Widespread Cervical Cancer Screening: Number of Cancers Prevented and Changes in Race-specific Incidence. Am. J. Clin. Oncol. *41*, 289–294.

Yao, Y., Xu, X., Yang, L., Zhu, J., Wan, J., Shen, L., Xia, F., Fu, G., Deng, Y., Pan, M., et al. (2020). Patient-Derived Organoids Predict Chemoradiation Responses of Locally Advanced Rectal Cancer. Cell Stem Cell *26*, 17–26.e6.

Please cite this article in press as: Lõhmussaar et al., Patient-derived organoids model cervical tissue dynamics and viral oncogenesis in cervical cancer, Cell Stem Cell (2021), https://doi.org/10.1016/j.stem.2021.03.012

STAR★METHODS

KEY RESOURCES TABLE

REAGENT or RESOURCE	SOURCE	IDENTIFIER
Antibodies		
Mouse anti-P63 antibody [4A4]	Abcam	Cat# ab735; RRID:AB_305870
Mouse anti-KI67 antibody [MM1]	Monosan	Cat# MONX10283; RRID:AB_1833494
Rabbit anti-PAX8 antibody	Proteintech	Cat# 10336-1-AP; RRID:AB_2236705
Mouse anti-keratin 13 antibody [1C7]	Progen Biotechnik	Cat# 10523; RRID:AB_1541007
Rabbit anti-keratin 14 antibody [Poly19053]	Covance	Cat# 905301; RRID:AB_2565048
Mouse anti-acetylated α Tubulin antibody [6-11B-1]	Santa-Cruz	Cat # sc-23950; RRID:AB_628409
Rabbit anti-CDKN2A/p16INK4a antibody [EPR1473]	Abcam	Cat# ab108349; RRID:AB_10858268
Chemicals, peptides, and recombinant proteins		
Nutlin-3a	Cayman Chemical	Cat# 10004372
Gemcitabine	Selleckchem	Cat# S1714
Cisplatin	Sigma	Cat# C2210000
Carboplatin	Selleckchem	Cat# S1215
Olaparib (AZD2281, Ku-0059436)	Selleckchem	Cat# S1060
Staurosporine	Sigma	Cat# 62996-74-1
Advanced DMEM/F12	Thermo Fisher	Cat# 12634010
HEPES	Thermo Fisher	Cat# 15630-056
GlutaMax	Thermo Fisher	Cat# 35050-038
Penicillin-Streptomycin	Thermo Fisher	Cat# 15140-122
R-spondin 1 (RSPO1)	made in-house	N/A
Noggin-Fc fusion protein	U-Protein Express	Cat# N002-100 ml
B27 supplement	GIBCO	Cat# 175044
A83-01	Tocris	Cat# 2939
N-Acetylcysteine	Sigma	Cat# A9165-5g
Nicotinamide	Sigma	Cat# N0636
Forskolin	Bio-Techne	Cat# 1099
ROCK inhibitor (Y-27632)	Abmole	Cat# Y-27632
p38 inhibitor (SB202190)	Sigma	Cat# S7067
FGF7	Peprotech	Cat# 100-19
FGF10	Peprotech	Cat# 100-26
EGF	Peprotech	Cat# AF-100-15
CHIR (Chir99021)	Stemgent	Cat# 04-0004-10
β-Estradiol	Sigma	Cat# E2257-1MG
Wnt surrogate-Fc fusion protein	U-Protein Express	Cat# N001-0.5mg
Primocin	InvivoGen	Cat# Ant-pm-1
Cultrex RGF BME type 2	Trevigen	Cat# 3533-005-02
Red Blood Cell Lysis Buffer	Roche	Cat# 11814389001
Cell Recovery Solution	Corning	Cat# 354253
TrypLE Express	GIBCO	Cat# 12605-010
Collagenase	Sigma	Cat# C9407
Dispase II	Thermo Fisher	Cat# 17105041
Colcemid	GIBCO	Cat# 15210-040

(*Continued on next page*)

Please cite this article in press as: Lõhmussaar et al., Patient-derived organoids model cervical tissue dynamics and viral oncogenesis in cervical cancer, Cell Stem Cell (2021), https://doi.org/10.1016/j.stem.2021.03.012

Continued

REAGENT or RESOURCE	SOURCE	IDENTIFIER
Vectachield HardSet Antifade Mounting Medium with DAPI	Vector Laboratories	Cat# H-1500-10
iQ SYBR Green Supermix	Bio-Rad	Cat# 1708887
Critical commercial assays		
MycoAlert mycoplasma detection kit	Lonza	Cat# LT07-318
RNeasy Mini Kit	QIAGEN	Cat# 74104
RNase-free DNase Set	QIAGEN	Cat# 79254
ReliaPrep gDNA Tissue Miniprep System	Promega	Cat# A2051
Zymogen Quick-DNA Microprep Kit	Zymo Research	Cat# D3021
GoScript Reverse Transcriptase Kit	Promega	Cat# A5003
CellTiter-Glo 3D Cell Viability Assay	Promega	Cat# G9683
Deposited data		
RNA-seq data	This study	GSE168244
WES data	This study	EGAS00001004439
Tumor and normal tissue-specific gene lists	This study	Table S2
Driver mutation list	This study	Table S3
Experimental models: cell lines		
Patient-derived cervical organoid lines	This study	Table S1
Mice		
NOD.Cg-Prkdcscid Il2rgtm1Wjl/SzJ (NSG) mice	The Jackson Laboratory	https://www.jax.org/strain/005557
Primers		
GAPDH fw	5′-GTCGGAGTCAACGGATT-3′	
GAPDH rev	5′-AAGCTTCCCGTTCTCAG-3′	
PAX8 fw	5′-AGCTGCCGACTAAGCATTGA-3′	
PAX8 rev	5′-GGGTGAGTGAGGATCTGCCA-3′	
MUC5B fw	5′-CAGAACCAGGCTGACGACTT-3′	
MUC5B rev	5′-ATGCAGTTCGAGTGGAAGGG-3′	
TP63 fw	5′-GACAGGAAGGCGGATGAAGATAG-3′	
TP63 rev	5′-TGTTTCTGAAGTAAGTGCTGGTGC-3′	
KRT13 fw	5′-GACCGCCACCATTGAAAACAA-3′	
KRT13 rev	5′-TCCAGGTCAGTCTTAGACAGAG-3′	
KRT14 fw	5′-GCAGCAGAACCAGGAGTACAA-3′	
KRT14 rev	5′-GAGGAGGTCACATCTCTGGAT-3′	
Software and algorithms		
LAS X software (version 1.1)	Leica	https://www.leica-microsystems.com/products/microscope-software/p/leica-las-x-ls/
ImageJ (version 1.51p)	NIH	https://imagej.nih.gov/ij/
Adobe Creative Cloud	Adobe	https://www.adobe.com/gr_en/creativecloud.html
GraphPad Prism (version 8.4.2)	GraphPad	https://www.graphpad.com/
Burrows-Wheeler Alignment (BWA, version 0.7.5)	Li and Durbin, 2009	N/A
Rstudio (version 3.6.2)	Rstudio	https://rstudio.com/
DESeq2 R package (version 1.18.0)	Love et al., 2014	N/A
VirusSeq software (VirusSeq-CLI wrapper tool)	Chen et al., 2013	https://github.com/UMCUGenetics/VirusSeq-CLI
ViFi software	Nguyen et al., 2018	https://github.com/namphuon/ViFi

(*Continued on next page*)

Continued

REAGENT or RESOURCE	SOURCE	IDENTIFIER
Bowtie 2 (fast gapped-read alignment)	Langmead and Salzberg, 2012	N/A
Sambamba (fast processing of NGS alignment formats)	Tarasov et al., 2015	N/A
GATK HaplotypeCaller (version 3.4-46)	DePristo et al., 2011	https://github.com/UMCUGenetics/IAP
Other		
AF7000 microscope	Leica	
DM4000 microscope	Leica	
Agilent2100 Bioanalyzer	Agilent	
Nanodrop Lite	Thermo Fisher	
Multi-drop Combi Reagent Dispenser	Thermo Fisher	
D300e Digital Dispenser	Tecan	
Spark multimode microplate reader	Tecan	
Bioanalyzer2100 RNA Nano 6000 chips	Agilent	Cat# 5067-1511

RESOURCE AVAILABILITY

Lead contact

Further information and requests for resources and reagents should be directed to and will be fulfilled by the lead contact, Hans Clevers (h.clevers@hubrecht.eu).

Materials availability

Distribution of organoids to third parties requires completion of a material transfer agreement and will have to be authorised by the Medical Ethical Committee UMCU to ensure compliance with the Dutch medical research involving human subjects' act. Use of organoids is subjected to patient consent; upon consent withdrawal, distributed organoid lines and any derived material will have to be promptly disposed of.

Data and code availaility

The accession number for the unprocessed WES data reported in this paper is EGA: EGAS00001004439. The accession number for the RNA-seq data reported in this paper is GEO: GSE168244.

EXPERIMENTAL MODEL AND SUBJECT DETAILS

Human material for organoid culture

All experiments with human tissue were approved by the medical ethical committee of the UMC Utrecht in accordance with all relevant ethical regulations. For initial establishment of the ectocervical organoid culture system, healthy cervical tissue was obtained anonymously from patients who underwent a hysterectomy performed for benign uterine diseases. Such protocol was valid temporarily for setting up the culture system and approved by the ethics committee (TCBio 17-127) of the Utrecht Medical Center, Utrecht, the Netherlands in compliance with guidelines from Ethical Committee and European Union legislation. Additionally, healthy cervical tissue (TCBio 14-472) and cancer tissue Pap brushes (TCBio 12-093) were obtained from ovarian and cervical cancer patients, respectively, under the designated ethical protocols. All patients participating in this study under the latter two protocols signed informed consent forms approved by the responsible authority. In all latter cases, patients can withdraw their consent at any time, leading to the prompt disposal of their tissue and any derived material.

Mice

For tumoroid transplantations, *NOD.Cg-Prkdcscid Il2rgtm1Wjl/SzJ* (NSG) female mice were used. Transplantation experiments were performed after institutional review by the Animal Ethics Committee of the Royal Netherlands Academy of Arts and Sciences (KNAW) with project license of AVD8010020151 and research protocol HI19.1004.

METHOD DETAILS

Healthy endo- and ectocervical organoid culture

Distinct digestion treatments were used for healthy endo- and ectocervical tissues. Endocervical tissues were first mechanically minced by scalpels, followed by digestion in collagenase solution (1 mg/mL of collagenase from *Clostridium histolyticum*, Sigma,

Please cite this article in press as: Lõhmussaar et al., Patient-derived organoids model cervical tissue dynamics and viral oncogenesis in cervical cancer, Cell Stem Cell (2021), https://doi.org/10.1016/j.stem.2021.03.012

Cat# C9407) for 1.5 hour at 37°C in a shaker. For ectocervical tissue, a slightly modified version of the previously published improved dissociation protocol was used (Fan et al., 2018). Briefly, healthy ectocervical tissue was dissociated with Dispase II solution in AdDF+++ (Advanced DMEM/F12 supplemented with 1x Glutamax, 10 mM HEPES and penicillin-streptomycin, all from Thermo Fisher) with 10 μM ROCK inhibitor (Abmole, Cat# Y-27632) overnight (16 hours) at 4°C on a tube roller. The ectocervical tissues were then incubated for an additional hour at room-temperature (RT) on a tube roller. Subsequently, the intact sheet of epithelium was peeled off from underlying connective tissue. The resulting sheets of ectocervical epithelium were subsequently mechanically minced by scalpels and subjected to dissociation with TrypLE (GIBCO, Cat# 12605-010) for 8-10 min at 37°C. After digestion procedure, in both cases resulting cell suspensions were washed three times with AdDF+++ and erythrocytes were lysed in Red Blood Cell Lysis Buffer (Roche, Cat# 11814389001). The cells were filtered through a 70 μm nylon cell strainer (Greiner, Cat# 542070) and collected via centrifugation for 5 min at 1200 rpm. Next, the cells were embedded into Basement Membrane Extract (Cultrex® BME RGF type 2, Trevigen, Cat# 3533-005-02) and plated in 30 μl-volume droplets on a pre-warmed 24-well suspension culture plates (Greiner, Cat# 662102) and allowed to solidify at 37°C for 30 min before addition of medium. The full growth medium (M7) for ectocervical organoids consisted of AdDF+++ supplemented with 1% Noggin conditioned medium (U-Protein Express, Cat# N002), 10% of RSPO1 conditioned medium (made in-house), 1x B27 supplement (GIBCO, Cat# 175044), 2.5 mM nicotinamide (Sigma, Cat# N0636), 1.25 mM n-Acetylcystein (Sigma, Cat# A9165), 10 μM ROCK inhibitor (Abmole, Cat# Y27632), 500 nM A83-01 (Tocris, Cat# 2939), 10 μM forskolin (Bio-Techne, Cat# 1099), 25 ng/ml FGF7 (Peprotech, Cat# 100-19), 100 ng/ml FGF10 (Peprotech, Cat# 100-26) and 1 μM p38 inhibitor SB202190 (Sigma, Cat# 7067). For endocervical cultures, M7 medium was additionally supplemented with 50 ng/μl EGF (Peprotech, Cat# AF-100-15), 100 nM β-Estradiol (Sigma, Cat# E2257) and two WNT pathway activators, i.e., 0.5 nM WNT surrogate (U-Protein Express, Cat# N001) and 0.3 μM CHIR (Stemgent, Cat# 04-0004-10). During the first 2-3 passages 100 μg/ml Primocin (InvivoGen, Cat# Ant-pm-1) was added to avoid contamination. For splitting, mechanical shearing through fire-polished plugged glass pipettes (Fisher Scientific, Cat# 11506973) can be used for endocervical cultures as the cystic organoids break easily. Due to the dense and hard-to-break properties of the ectocervical organoids, dissociation with TrypLE for 20 min at 37°C is required. After splitting, the plating density for ectocervical lineage should stay between 5000-10000 cells/30 ul drop for optimal outgrowth. The approximate splitting ratio is 1:4 and 1:10 in every two weeks for endo- and ectocervical lines, respectively. All organoid lines tested negative in the MycoAlert mycoplasma detection kit (Lonza, LT07-318). Following this protocol, organoids could be derived with 82% (10/12) and 93% (25/27) success rate in endo- and ectocervical lineage, respectively. Patient clinical data for the 6 more thorougly characterized healthy lines in this study is presented in Table S1.

Tumor-derived organoid (tumoroid) culture

Cervical tumor tissues were obtained from consenting patients via Pap-brush method. The Pap-brush was tipped in a tube filled with AdDF+++ to release the tissue fragments from the brush. The tissue fragments were then pelleted and digested in collagenase solution (specified above) for 40 min at 37°C in a shaker. The suspension was then additionally mechanically sheared via a glass-pipet and the cell clumps pelleted via centrifugation for 5 min at 1200 rpm. Before plating the erythrocytes were lysed as described above. The resulting small tissue fragments were then embedded into BME on suspension plates and covered with the full growth medium (specified above). Tumoroid derivation success rate was 46% (12/26 Pap-brushes). Patient clinical data is presented in the Table S1.

Organoid formation efficiency assay

Fresh tissue was digested (see Methods above) and the material dissociated into single cells using TrypLE for 10-15 min at 37°C. Cells were then washed in AdDF+++ and passed through a 70 μm nylon cell strainer to ensure the single-cell suspension. Cells were counted using haemocytometer. For the growth factor requirement experiment (Figure 1B), 5000 cells were plated per 30 μL BME drop into 24-well suspension plate and overlayed with 500 μL of medium. For organoid formation efficiency assay (Figure 1C), 1000 cells were plated into 5 μL BME drops into 48-well suspension plate (Greiner, Cat# 677102) and overlayed with 250 μL of medium. The number of organoids was scored 10 days post-seeding. Cystic endocervical organoids were scored if there were visible lumens observed. Dense ectocervical organoids were scored if the structure contained 2 or more layers ($\geq$80 μm in size). Data analysis was performed by using ImageJ software and the experiments were performed in at least 2 biological replicates (2 technical replicates per biological replicate, n $\geq$ 4).

HSV-1 infection and quantification experiments

For the virus infection assays, dtTomato-tagged HSV-1 virus was used. The virus was a kind gift of Prashant Desai (John Hopkins University, Baltimore, MD). Three days after splitting, the organoids were exposed to 1 × 10^7 PFU HSV-dTomato virus in medium suspension and incubated for 6 hours. After the exposure, the organoids were collected and washed with 10 mL of DMEM. The organoids were plated (1,500 organoids in 20 μL BME per well) in 48-well format. Organoids were kept in full organoid medium, and DNA was harvested at several time points throughout a week. For DNA collection, the medium was removed and organoids pelleted by centrifugation in a 15 mL falcon tube. The pellet was stored at −20°C until gDNA extraction. For DNA quantification, qPCR reactions were performed in 384-well format using IQ SYBR Green Mix (Bio-Rad) in the presence of 0.67 μmol/L forward and reverse primer and 2% of total DNA isolated from 1,500 organoids. After gDNA extraction, qPCR was performed with the following primers to detect HSV DNA: forward: 5′-ATCAACTTCGACTGGCCCTT-3′ and reverse: 5′-CCGTACATGTCGATGTTCAC-3′. PCR program used: 2 minutes at 95°C and for 40 cycles at: 15 s at 98°C, 15 s at 60°C, and 15 s at 72°C. Increase in DNA content was calculated

relative to noninfected wells. Timelapse brightfield and dtTomato imaging was performed on a Leica AF7000 fluorescent microscope equipped with a Leica DFC420C camera at 37°C and 5% humidified CO_2.

Karyotyping

About 5-6 days after splitting of the organoids, the cultures were treated with 0.1 μg/mL colcemid (GIBCO, Cat# 15210-040) in the culture media for 16h at the 37°C cell incubator (with 5% CO_2). Organoids were then collected and dissociated into single-cells using TrypLE. Hypotonic shock was performed by drop-wise addition of pre-warmed 75 mM KCl and incubated at 37°C for 10 min. The swollen cells were fixed by slow drop-wise addition of ice-cold methanol:acetic acid (3:1) while gently tapping the cell suspension. Following three rounds of fixation and washing steps, the cell suspensions were dropped on a glass slide from the height of at least 1 meter, air-dried and mounted with DAPI-containing Vectashield (Vector Laboratories, Cat# H-1500-10). The slides were imaged on AF7000 microscope (Leica) with a 100x objective, and quantified by manual chromosome counting. At least 15 spreads were analyzed per organoid line.

Immunohistochemistry

Tissues were fixed overnight in 4% paraformaldehyde (PFA) at 4°C followed by dehydration and paraffin embedding. To prepare organoids for histological stainings, intact BME-drops containing organoids were collected from the culture plates and incubated in 5 mL Cell Recovery Solution (Corning, Cat# 354253) on ice for 30 min, occasionally inverting the tube, to dissolve BME. Organoids were then allowed to settle to the bottom of the tube by free gravitation and the supernatant was removed by pipetting. Next, the settled organoids were suspended in 4% PFA at RT for 1h for fixation, followed by washing with PBS. Finally, the processed organoids were embedded into paraffin blocks. Sections were cut and hydrated before staining. Sections were subjected to H&E and PAS staining or immunohistochemical staining by using overnight incubation with antibodies raised against TP63 (Abcam, Cat# AB735, 1:800), MKI67 (Monosan, Cat# MONX10283, 1:2000), PAX8 (Proteintech, Cat# 10336-1-AP, 1:2000), KRT13 (Progen Biotechnik, Cat# 10523, 1:100), KRT14 (Covance, Cat# 905301, 1:2000), acetylated α Tubulin (Santa-Cruz, Cat# sc-23950, 1:2000) and p16INK4a (Abcam, Cat# ab108349, 1:500). For most antibodies, antigen retrieval was performed in citric acid solution (pH 6.0), except for p16INK4a antibody that required TRIS/EDTA (pH 9.0) treatment. Images were acquired on DM4000 microscope (Leica) and processed using Leica LAS X software.

RNA isolation, cDNA preparation and RT-qPCR

For RT-qPCR analysis, RNA was isolated from cervical organoids and tissues using the RNeasy Mini Kit (QIAGEN, Cat# 74104) following the manufacturer's instructions including DNaseI treatment (QIAGEN, Cat# 79254). Next, RNA was reverse transcribed from 500 ng of total RNA using GoScript Reverse Transcriptase Kit (Promega, Cat# A5003) and random Oligo$(dT)_{15}$ Primer (Promega, Cat# C1101). Quantitative PCR was performed with three biological replicates in duplicates using the indicated primers listed in the Key Resources Table, SYBR Green Supermix (Bio-Rad, Cat# 1708887) and Bio-Rad systems. Gene expression was quantified using the delta-delta-Ct method and normalized against GAPDH housekeeping gene.

Bulk RNA-seq analysis

For RNA-seq analysis, RNA was isolated from organoids and tissues using the RNeasy Mini Kit (QIAGEN, Cat# 74104) following the manufacturer's instructions including DNaseI treatment. RNA integrity was confirmed by Agilent 2100 bioanalyzer. The libraries were prepared by the Utrecht Sequencing Facility (USEQ) based on polyA enrichment. Sequencing was performed on an Illumina NextSeq500 by using 75-bp single- or paired-end sequencing. Single- and paired-end reads were aligned to the human reference genome (GRCh37) using Burrows-Wheeler Aligner (BWA) (v0.5.9) (Li and Durbin, 2009). DESeq2 (v1.18.0) package (Love et al., 2014) was used to normalize count data and for differential gene expression analysis in Rstudio (R v3.6.2, Bioconductor v3.10 (BiocManager v1.30.10)).

Viral subtype detection and integration analysis

Viral sequences of different HPV subtypes were detected in the RNA-seq data of the different tumoroid lines by using VirusSeq-CLI, a wrapper around the VirusSeq pipeline (Chen et al., 2013). VirusSeq-CLI can be accessed through the following website: https://github.com/UMCUGenetics/VirusSeq-CLI. For all tumoroid lines, VirusSeq-CLI was used with default parameters and the top hit with more than 1,000 counts was reported. Integration sites were identified by using ViFi (Nguyen et al., 2018). ViFi can be accessed through the following website: https://github.com/namphuon/ViFi. For all tumoroid lines, ViFi was used with default parameters.

Viral transcriptome analysis

The genomes of HPV subtypes HPV16, HPV18, HPV30 and HPV45 were downloaded from the Papillomavirus Episteme (PaVE) (Van Doorslaer et al., 2017). RNA-seq data from each tumoroid (early and late passages) and tissue samples were mapped to the corresponding HPV subtype with Bowtie2 (v2.3.5.1) (Langmead and Salzberg, 2012) and depth analysis for each mapped sample was performed with sambamba (v. 0.6.5) (Tarasov et al., 2015).

DNA extraction and whole-exome sequencing analysis

Genomic DNA was isolated from both tissues and tumoroids using Reliaprep gDNA Tissue Miniprep System (Promega, Cat# A2051) according to the manufacturer's protocol. Genomic DNA from the patients' blood samples was extracted using Zymogen Quick-DNA Microprep Kit (Zymo Research, Cat# D3021). The whole exome sequencing (WES) was performed at Macrogen Inc. (Seoul, South Korea) using Agilent SureSelect V7 8Gb 150bp PE Novaseq exome. WES data was mapped against human reference genome GRCh38 by using BWA (v0.7.5) mapping tool (Li and Durbin, 2009) with settings 'bwa mem -c 100 -M'. Sequence reads were marked for duplicates by using Sambamba (v0.6.8) and realigned per donor by using Genome Analysis Toolkit (GATK) IndelRealigner (v3.8.1). Raw variants were multisample-called by using the GATK HaplotypeCaller (v3.8-0) (DePristo et al., 2011) and GATK-Queue (v3.8-0) with default settings and additional option 'EMIT_ALL_CONFIDENT_SITES'. The quality of variant and reference positions was evaluated by using GATK VariantFiltration (v3.8-0) with options '-snpFilterName LowQualityDepth -snpFilterExpression "QD < 2.0" -snpFilterName MappingQuality -snpFilterExpression "MQ < 40.0" -snpFilterName StrandBias -snpFilterExpression "FS > 60.0" -snpFilterName HaplotypeScoreHigh -snpFilterExpression "HaplotypeScore > 13.0" -snpFilterName MQRankSumLow -snpFilterExpression "MQRankSum < −12.5" -snpFilterName ReadPosRankSumLow -snpFilterExpression "ReadPosRankSum < −8.0" -cluster 3 -window 35'. Full pipeline description and settings also available at: https://github.com/UMCUGenetics/IAP.

To obtain potential driver mutations and reduce the number of false positive calls, we further filtered with the following criteria: passed by VariantFiltration with a base coverage of at least 10X, HIGH or MODERATE expected effect on the gene reported by SnpEff annotation, no overlap with single nucleotide polymorphisms (SNPs) in the Single Nucleotide Polymorphism Database (v146) nor with the panel of normals (VCF-file available upon request); and absence of the variant in a panel of unmatched normal human genomes (BED-file available upon request) and not RefSNP number has been assigned except for the variants with both RefSNP ID's and COSMIC ID's (well-known drivers). Shared mutations between patients were also excluded as artifacts. The potential driver mutations for each sample are listed in Table S3.

In vitro drug screen

Two days prior to the start of the drug exposure, organoids were disrupted into single cells using TrypLE and filtered using a 70-mm nylon cell strainer. Cells were counted and resuspended in 5% BME/growth medium (25,000 cells/mL) prior plating in 40 μL volume in 384-well plates (Corning, Cat# 4588) by using Multi-drop Combi Reagent Dispenser (Thermo Fisher, Cat# 5840300). Two days after plating the cells, the drugs were added using the D300e Digital Dispenser (Tecan). Nutlin-3a (Cayman Chemical, Cat# 10004372), gemcitabine (Selleckchem, Cat# S1714) and olaparib (Selleckchem, Cat# S1060) were dissolved in DMSO. Cisplatin (Sigma, Cat# C2210000) and carboplatin (Selleckchem, Cat# S1215) were dissolved in PBS containing 0.3% Tween-20 (Sigma, Cat# P1379), which was required to dispense these drugs using the HP printer. All wells were normalized for solvent used. DMSO percentage never exceeded 1%, PBS/Tween-20 percentage never exceeded 2%. Drug exposure was performed in triplicates for each concentration shown. Five days (120 hours) after adding the drugs, ATP levels were measured using the CellTiter-Glo 3D Viability Assay (Promega, Cat# G9683) according to the manufacturer's instructions, and luminescence was measured using a Spark multimode microplate reader (Tecan). Results were normalized to vehicle (100%) and baseline control (Staurosporine 1 μmol/L (Sigma, Cat# 62996-74-1); 0%).

In vivo xenotransplantation assays

The tumoroid lines were split 3-4 days before transplantation by dissociating them into single-cell suspension. On the day of the transplantation, the small organoids were released from BME and small proportion of the total sample was dissociated into single cells to estimate the cellular density of each sample. Approximately 200 000 cells were suspended in 50 μL of medium mixed with BME at a 1:1 ratio. Subcutaneous injections were performed into opposite flanks of all 4-5 NSG mice per line (2 flanks per mice, 200 000 cells/50 μL per location). The mice were sacrificed 3-4 months (90-120 days) after injections. Tumor measurements were taken by digital calipers (RS PRO, Cat# 841-2518) and volumes estimated by formula: tumor volume = (length x width^2)/2, where length represents the largest tumor diameter and width the perpendicular tumor diameter. All tumors were subjected to immunohistochemical analysis.

QUANTIFICATION AND STATISTICAL ANALYSIS

The experiments described in this study are based on the analysis of at least 3 different organoid lines derived from 3 independent donors. Statistical methods are specified under respective figure legends where applicable. Statistical analyses were performed with MS Excel and GraphPad Prism. P values were calculated using two-tailed Student's t test assuming a normal sample distribution, error bars represent either ± SEM or ± SD as specified in the legend. RNA-seq and WES data were mapped by BWA method. RNA-seq data was normalized by DESeq2 and analyzed in Rstudio. WES data filtering criteria is described in detail under the STAR Methods section. Blinded evaluation of tumoroids and tumors was performed by expert pathologist.